DESIGN OF LOW-POWER RF ENERGY HARVESTER FOR IOT SENSORS

A Dissertation
presented to
the Faculty of the Graduate School
at the University of Missouri

In Partial Fulfillment
of the Requirements for the Degree
Doctor of Philosophy

by
DILRUBA PARVIN
Dr. Syed K. Islam, Dissertation Supervisor
DECEMBER 2022

The undersigned, appointed by the dean of the Graduate School, have examined the dissertation entitled

DESIGN OF LOW-POWER RF ENERGY HARVESTER FOR IOT SENSORS

presented by Dilruba Parvin,

a candidate for the degree of Doctor of Philosophy in Electrical and Computer Engineering,

and hereby certify that, in their opinion, it is worthy of acceptance.

Dr. Syed K. Islam

Dr. Dominic K. C. Ho

Dr. Justin Legarsky

Dr. Abu Saleh Mohammad Mosa

DEDICATION

To my beloved father

Md Delwar Hossain

My beloved mother

Salina Parvin

My brothers

Sheikh Md Abdullah and Iqtidar Hossain

ACKNOWLEDGEMENTS

I wish to express my sincere gratitude to Dr. Syed Kamrul Islam for the support and guidance throughout all these years of my doctoral program. Without his encouragement and directions, my academic and professional achievements would not have been possible. I am very grateful to Dr. Dominic K.C. Ho, Dr. Justin Legarsky, Dr. Abu Saleh Mohammad Mosa for serving on my doctoral committee and for providing valuable insights and guidance.

I am also grateful to my mentors Dr. Samira Shamsir, and Omiya Hassan for their guidance during my early stage of research. It was also great to work with Md. Maruf Hossain Shuvo, Mengrui Chen, Twisha Titirsha and Nazmul Amin. I would like to thank my friends Ummul Afia Shammi, Tanmoy Paul, Md. Mohimanul Islam for making my time in MU enjoyable.

I am also thankful to the faculty and staffs of the EECS department of University of Missouri, specially Dr. Yi Shang, Joanna Chandler and Patimat M. Magomedova for their continuous support.

Last but not the least; I would like to thank my family members for their enormous support. I would like to thank my father for always being so supportive and encouraging. From him I learnt how to dream big and make that happen without any fears. I would like to thank my mother for always encouraging me and giving me strength that is required to pursue my dream. I would like to thank my brothers for always being there for me and putting smile on my face even during the toughest time. I also would like to thank my friends, Sushmita Joardar, Mushfiq Ayon and Tanveer Ahmed Siddiqui for always being there for me and for going up and beyond to help me out. I had to do all the works that were required to pursue a Ph.D., but I got the support required to complete a Ph.D. program from my family and friends.

TABLE OF CONTENTS

DESIGN OF LOW-POWER RF ENERGY HARVESTER FOR IOT SENSORS

Dilruba Parvin

Dr. Syed K. Islam, Dissertation Supervisor

ABSTRACT

Rapid technological advancement in CMOS technologies has resulted in increased deployment of low-power Internet-of-Things (IoT) devices. As batteries, used to power-up these devices, suffer from limited lifespan, powering up numerous devices have become a major concern. Radio frequency (RF) is ubiquitous in the surroundings from which energy can be harvested and utilized to increase battery lifetime. Even for low-power sensors, RF energy harvesters can be utilized as primary power sources. However, power density of RF signals is very low and therefore building blocks of RF energy harvester need to be designed carefully to maximize efficiency to gain suitable output power.

This research is focused on the design of an RF energy harvesting system in standard CMOS technology. The main goal of this research is to design an RF energy harvesting system with high power conversion efficiency (PCE) and adequate output voltage for low input power. The proposed dynamic voltage compensated cross-coupled fully differential rectifier is capable of providing very high PCE. The synchronous DC-DC boost converter provides stable DC output voltage. Rectifier and DC-DC converter of the system have been designed by using low-power transistors to ensure operation at very low input power. In order to maximize the power transfer through the system, matching network and maximum power point tracking (MPPT) controller has been implemented. In order to cope with rapid input power variation, a machine learning (ML) based MPPT controller has been designed and implemented into FPGA. The proposed ML based MPPT controller has demonstrated fast response time. To further enhance the performance of the RF energy harvesting system, a self-compensated rectifier integrated energy harvesting system is also presented. The energy extracted by using the proposed RF energy harvesting systems can easily be stored and utilized to fully power up low-power sensors used for IoT devices. Integration of RF energy harvester with these devices will significantly reduce the maintenance cost and result in energy-effluent IoT technologies.

Chapter 1

INTRODUCTION

1.1 Motivation

Rapid growth of world's population and tremendous pace of technological innovation resulted in rapid surge in energy demand. For power supply, modern technology is largely dependent upon energy sources found on earth such as coal, oil and natural gas. To meet the skyrocketing energy demand, energy production has been increased more than 2.5 times since 1971, from 5485 Megatons of oil equivalent (Mtoe) to 14,282 Mtoe in 2018 [1].

In Fig. 1.1, world energy supply trend for the year 1973 and 2020 is demonstrated. Although fossil fuel is still considered to be the principal source of energy, the available sources are already getting depleted while the exploration of new sources is becoming cumbersome and expensive causing great danger to the environment. This has led to the exploration of alternate and renewable sources of energy. Renewable sources are considered to be alternative to the traditional fossil fuels and tend to be much less harmful to the environment. Since the energy crisis in 1973, implementation of several alternative energy sources such as wind energy, solar energy, nuclear energy have been increased to meet this energy demand. To reduce global warming effect generated by production of energy from fossil fuel, research on renewable energy has also been drawn attention. Harvesting of the wasted forms of energy is of great interest to energy research community as the focus has been shifted to green, clean and efficient energy production while meeting the increased energy demand for rapid technological innovation.

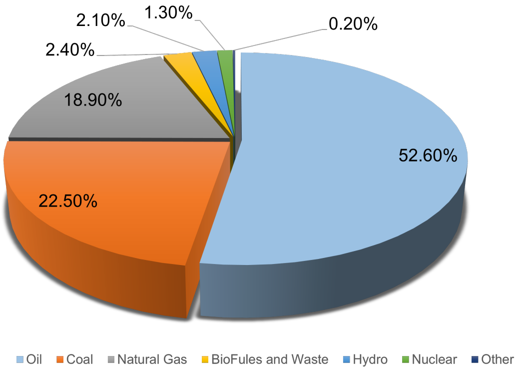

(a) 1973

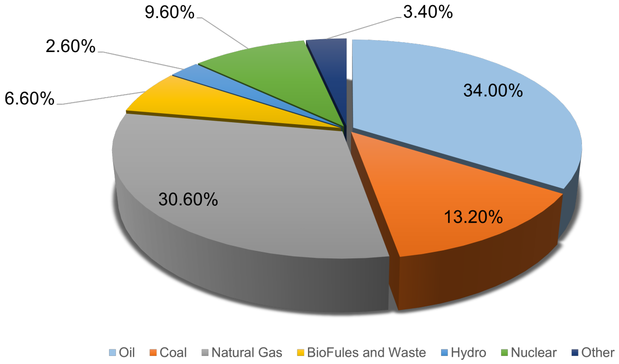

(b) 2020

Figure 1.1: World energy consumption by the year 1973 and 2020 [2].

1.2 Energy Flow Trend

In this modern age of technology, energy is required in almost every aspects of life such as for transportation and commercial applications. These energy demand are met by energy sources such as fossil fuels, hydroelectric, solar and geothermal. In the process of producing and delivering energy from the sources to the user end, a significant amount of energy is being wasted in the form of thermal or acoustic energy.

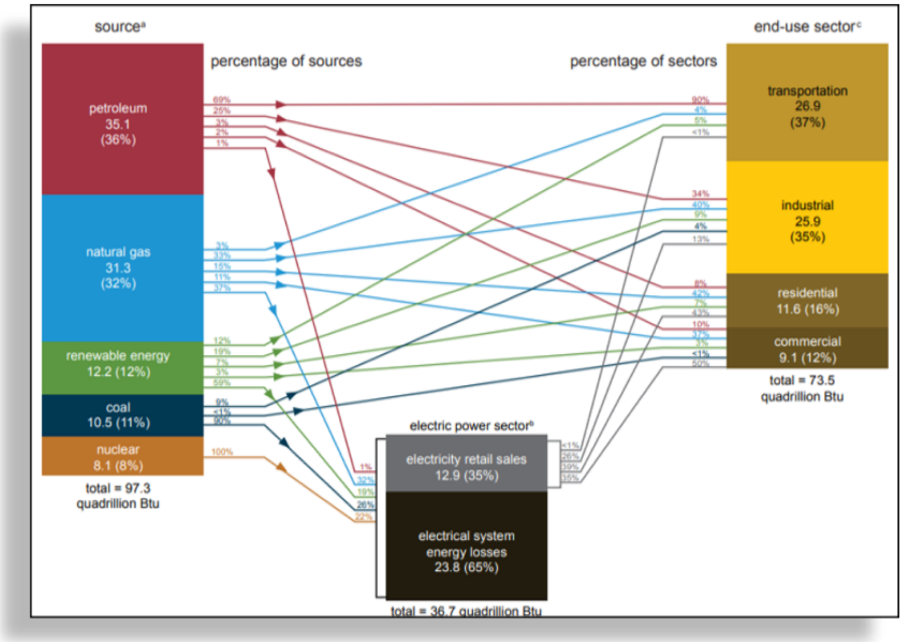

Figure 1.2: Energy flow by source and sector, 2021 in the US (in Quadrillion BTU) [3].

Fig. 1.2 presents energy flow trend from source end to user end for the year 2021. From the figure it can be concluded that transportation and electric power sector consume the majority amount of power. Fig. 1.3 demonstrates the energy flow from production end to consumption end in the United States in the year 2021 [4]. From this figure it can be observed that petroleum, coal, natural gas and nuclear are considered as major energy sources. The energy required in the transportation sector is 26.9 quadrillion British Thermal Unit (BTU) of which 24.3 quadrillion BTU is being produced solely by petroleum. However, only 5.65 quadrillion BTU energy is being used properly while 21.2 quadrillion BTU energy is being wasted. For electricity generation 36.6 quadrillion BTU energy are being generated from various energy sources such as solar, nuclear, hydroelectric, wind, natural gas and geothermal. Approximately 12.9 quadrillion BTU energy is utilized properly whereas 23.7 quadrillion BTU energy are wasted as well. In 2021, United States generated 97.3 quadrillion BTU of energy from which 31.8 quadrillion BTU was properly used by the consumers while approximately 65.4 quadrillion BTU energy was wasted in the process. Thus it can be concluded that approximately 67% of total energy being produced are being wasted or rejected during the delivery process. This tremendous loss of energy is caused due to inefficient system design. On the other hand, approximately 13% of the world's population (940 million people) do not have access to electricity which drastically affects their living quality, health, education[5]. Conversion of wasted energy into usable energy is a sustainable solution of the emerging energy crisis.

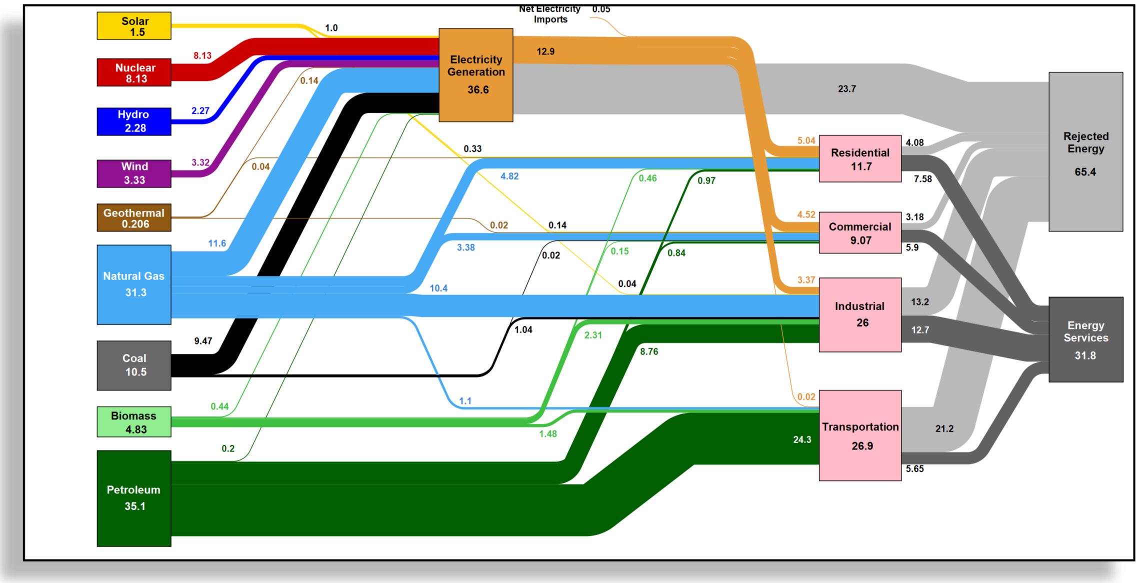

Figure 1.3: Energy production, usage, and utilization flow chart in the United States in 2021 (unit in quadrillion BTU) [4].

1.3 Energy for IoT Devices

Internet of Things (IoT) systems employ numerous devices which are connected through internet providing these devices with ability to collect and exchange data from one another as well as from user interactions. IoT technology is moving towards a connected life which includes home automation, smart roads, smart wearables, connected health and connected wearables. By reducing the gap between the physical and the digital worlds, IoT is expected to make life more convenient and productive. The global market of IoT devices is projected to reach to a size of $35.2 billion by the year 2025, as illustrated in Fig. 1.4.

Sensor networks of IoT are typically battery powered. Due to the limited lifetime of the batteries, manpower is needed for their periodic replacement and maintenance resulting in increased cost.

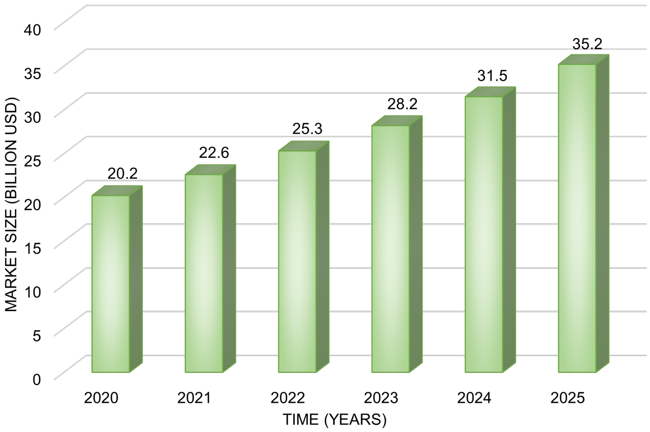

Figure 1.4: Global market of Internet of Things (IoT) in energy market.

In addition, battery replacement incurs higher cost when IoT devices are placed in remote areas. Besides, batteries typically contain chemicals and metals which can be hazardous to environment.

A suitable alternative is to use energy harvesting-powered sensor which makes it autonomous resulting in a lower maintenance cost. Further, energy harvesters are easier to install than batteries lowering the installation cost. Thus, with the rapid growth of IoT technologies, the demand for wireless sensor network equipped with energy harvesters is also increasing. Energy harvesting can play a vital role in fulfilling the growing demand of sustainable energy and is capable of providing safe and power efficient systems which require minimum or low maintenance. Besides, growing need to minimize carbon emission and effects of climate change are working as driving forces behind the growth of energy harvesting market.

1.4 Research Goal

The goal of this research is to design a low-power RF energy harvesting system to extract energy from 900 MHz RF signal. For the low-power RF energy harvesting system, a dynamic-bias compensated RF rectifier with a off-chip matching network and a synchronous DC-DC boost converter is presented. To ensure maximum power transfer from the receiver to the DC-DC converter, fractional open-circuit voltage (FOCV) algorithm and neural network based maximum power point tracking (MPPT) systems were implemented. To perform with high efficiency at very low input-power, a self-compensated RF rectifier with off-chip matching network is also developed and presented in this dissertation.

1.5 Dissertation Outline

The remaining chapters of this research will cover followings. In Chapter 2, general architecture of energy harvesting system, various sources of harvesting energy as well as latest technologies of radio frequency based energy harvesting system are presented. Chapter 3 presents the proposed RF energy harvesting system. Design and functionality of each building block of RF energy harvesting system with detailed analysis of results are also included in this chapter. In Chapter 4, design and analysis of a novel self-compensated RF energy harvesting system are presented. Concluding remarks and future direction of research have been added in Chapter 5.

Chapter 2

RADIO FREQUENCY BASED ENERGY HARVESTING TECHNOLOGIES

2.1 Architecture of Energy Harvesting System

Energy harvesting is a method of converting the available energy from the surroundings into a usable electrical energy to create a maintenance-free and sustainable form of energy. By recycling already produced and wasted energy, energy harvesting offers to be a sustainable solution to meet the gap between energy demand and energy supply. Upon implementing with environmental monitoring nodes, energy harvesting systems can extract energy from the environment and can be used to power the nodes of environmental wireless sensor networks (EWSNs) improving their performance or extending their lifetime. Tremendous amount of energy is present in our surroundings such as light, kinetic, electromagnetic, thermal, chemical etc. Table 2.1 presents the power density of the energy sources available in nature.

Fig. 2.1 depicts the building blocks of a typical energy harvesting system. Energy generated from

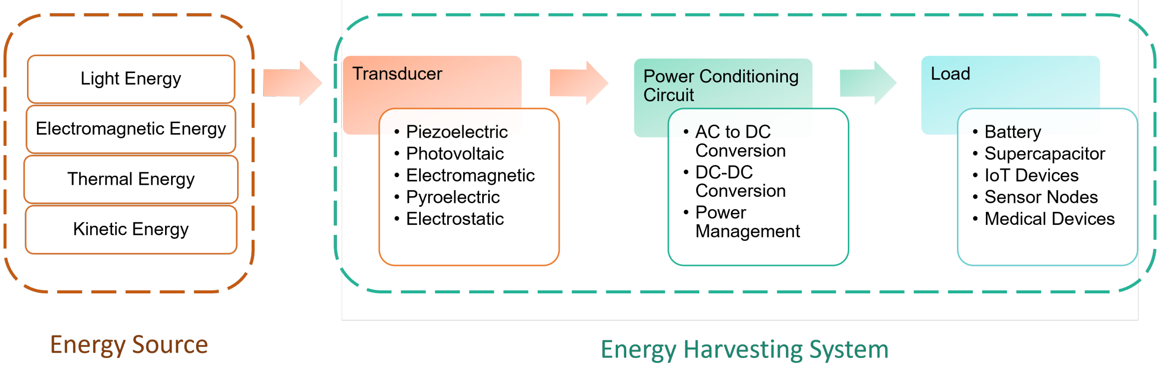

Figure 2.1: Building blocks of energy harvesting system.

Table 2.1: Power density of ambient energy sources[6]

Harvest Method	**Working Principal**	**Power Density**
Solar Energy	Photovoltaic	15-100 mW/cm3 - bright day
Solar Energy	Photovoltaic	0.15-100 µW/cm3 - cloudy day
Kinetic Energy	Piezoelectric	200 µW/cm3
Thermal Energy	Pyroelectric	10 µW/cm3
Ambient RF	Rectenna	0.1 µW/cm3-GSM 900
Acoustic Noise	PZT	0.003 µW/cm3 – 75 dB

an already existing energy source such as light or thermal energy is converted into electrical form by using a photovoltaic or pyroelectric transducer. The main concern while designing energy harvesting system is the gap between the voltage being produced by the transducer and the minimum amount of voltage required by the load. This gap can be fulfilled by using power conditioning circuits such as AC-DC conversion circuit, DC-DC conversion circuit or power management circuit. Finally, there is the load such as battery, super capacitor, IoT devices in which the converted usable electrical energy is fed to increase their performance.

2.2 Methods for Energy Harvesting

Based of the type of energy being extracted, the transducers, power management circuits, applications architectures needs to be determined. Therefore, having knowledge regarding the harvesting methodology of the energy sources is imperative.

2.2.1 Thermal Energy Harvesting

Thermal energy is one of the most commonly available energy in the surroundings making it a viable source for harvesting energy. In thermal energy harvesting, temperature difference is converted into electrical energy. Wasted thermal energy from furnaces, heater and auto engines can be converted into usable electrical energy by utilizing thermoelectric, thermocoupling and pyroelectric properties of materials.

Thermoelectric effect is known as the direct conversion between thermal energy and electrical

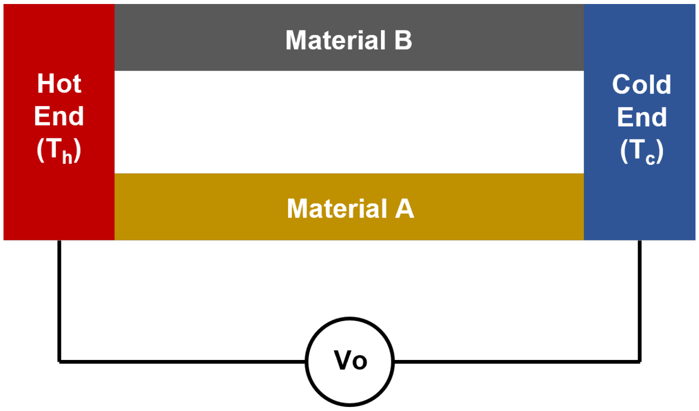

Figure 2.2: Seeback effect.

energy. When a junction of two different materials are heated, an electromotive force occurs, causing a small voltage potential. Upon being connected to an electric circuit, a DC current will flow through that circuit. This phenomenon is known as Seeback effect. Fig. 2.2 presents the Seeback effect generated when two thermoelectric materials are joined together with hot (temperature T_h) and cold (temperature T_c) juctions. Seebeck EMF of V_o is obtained across the junctions.

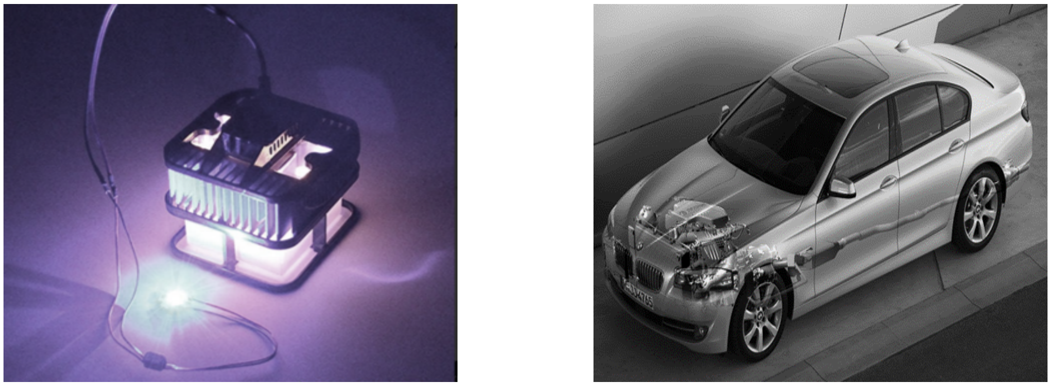

(a) ThermaWatt, a candle powered TEG.

(b) TEGs to be used on BMW cars.

Figure 2.3: Commercial TEGs.

The output voltage, V_o can be expressed as:

$$V_o = m\alpha\Delta T_G \tag{2.1}$$

Where

- m represents the number of thermocouplers,
- α represents relative Seeback coefficient, and

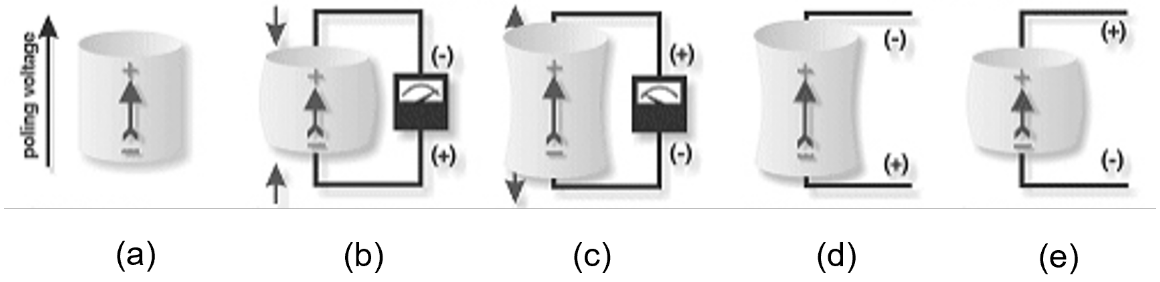

(a) (b) (c) (d) (e)

Figure 2.4: Generator and motor action of piezoelectric element: (a) disk after polarization, (b) disk compressed, (c) disk stretched, (d) disk lengthens, and (e) disk shortens [10].

- ΔT_G represents temperature difference between hot and cold junctions.

Fig. 2.3 presents commercially available thermoelectric generators (TEG). Fig. 2.3 (a) presents a Thermawatt that converts the heat of a candle into electricity and produces an output power of 500 mW at room temperature [7]. Fig. 2.3 (b) presents the application of TEGs into BMW cars [8]. Electricity is being generated from the wasted heat of the automotive engine to improve the efficiency of the engine.

2.2.2 Piezoelectric Energy Harvesting

Piezoelectric transducers convert the vibrational energy available in nature into electrical energy. When mechanical stress is applied on piezoelectric materials, an electric field is generated [9] which can be utilized to harvest the energy. Generally, piezoelectric materials are crystals or ceramics. Polycrystalline lead titanate (PZT) has high piezoelectric coefficient and low fabrication cost. Therefore, PZT is one of the most commonly used materials for energy harvesting.

When stress is applied on a piezoelectric material, the positive and the negative charge centers of the crystal are misaligned which causes deviation form their equilibrium states. This results in internal polarization. Adjacent internal dipoles of the material neutralize each other except the dipoles on the surface. Therefore, an overall electric potential is generated across the thickness of the material. On the other hand, applying electric field to the material will cause displacement of the charge center of the atoms resulting in deformation of the material.

In the case of piezoelectric materials, values of the compressive stress and the voltage generated by applying stress to a piezoelectric material are linearly proportional up to a material-specific stress. This is also applicable for applied voltage and generated strain.

If a piezoelectric material is compressed along the direction of polarization, a voltage of the same polarity with poling voltage is generated (Fig. 2.4 (b)). If tension is applied along the direction of

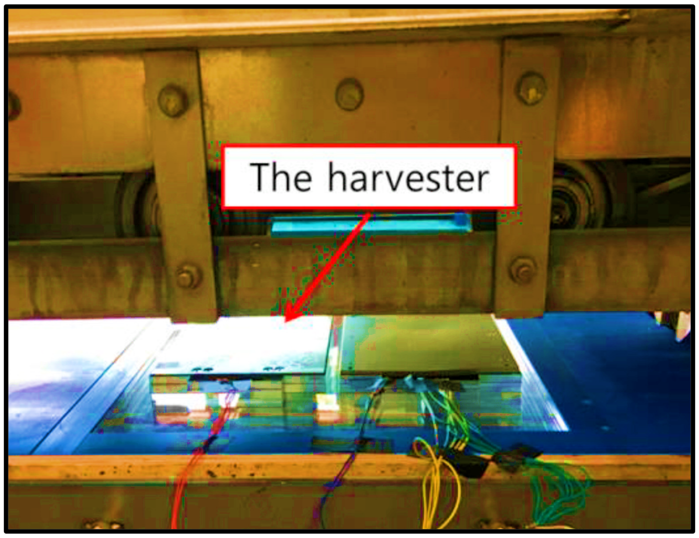

Figure 2.5: Piezoelectric energy harvesting for road highway [11].

polarization, a voltage of the opposite polarity with the poling voltage is generated (Fig. 2.4 (c)).

If a voltage of the same polarity as the poling voltage is applied to a piezoelectric material, the material will lengthen in the direction of poling voltage (Fig. 2.4 (d)) and vice versa (Fig. 2.4 (e)).

The electrical behavior of a material can be expressed by Hooke's law:

$$D = \epsilon E \tag{2.2}$$

Where

- D represents displacement of charge density,
- ϵ represents permittivity, and
- E represents applied electric field strength.

For a system Hooke's law can be expressed as the following [12]:

$$S = sT \tag{2.3}$$

Where

- S represents strain,
- s represents compliance, and
- T represents stress.

The direct and converse piezoelectric effect can be represented as:

$$D = dT + \epsilon E \tag{2.4}$$

$$S = sT + dE \tag{2.5}$$

Fig. 2.5 presents an impact-based piezoelectric road energy harvester for smart highways with maximum output power of 483 mW. The limitations of piezoelectric energy harvesters are their frequency dependency and inefficiency at low-frequency human motion.

2.2.3 RF Energy Harvesting

In this era of internet, electromagnetic waves are omnipresent in our surroundings. Cell phones, GSM routers, WLAN routers and TV towers transmit radio waves of various frequencies. Compared to solar and thermal energies, radio frequency energy is continuously available in both indoor and outdoor environments [13]. The radio waves ranging from 3 kHz to 300 GHz are utilized for energy harvesting [14].

These radio waves can be converted into electric power by using a receiving antenna. In RF energy harvesting, electromagnetic radiation emitted from an ambient RF source is received by a receiving antenna and is converted into usable electric power. Radio frequency is an appropriate source for energy harvesting due to its presence everywhere in various forms.

Sensor nodes employed to monitor environmental data such as temperature, moisture, air quality as well as proximity have two operation modes: (a) active and (b) sleep. The sensors remain in the sleep mode most of the time. Upon receiving a certain voltage level, the sensors operate in active mode. Most of the time these sensors are placed into remote and dangerous places. Powering up these sensors using batteries is cumbersome and require in-person maintenance and thus increases the cost. Application of RF energy harvesting systems with these sensors will increase the lifetime of the battery enhancing the overall performance.

Fig. 2.6 presents the RF sources available in the environment. Fig. 2.7 shows the frequencies of the RF sources. RF energy harvesters can extract energy from dedicated RF sources. The amount of RF power transmitted at a particular frequency is specified by Federal Communication Commission (FCC). Generally, FM, TV and GSM signals require licence to transmit RF signals. However, for industrial, scientific and medical (ISM) purposes parts of frequency signals are internationally reserved

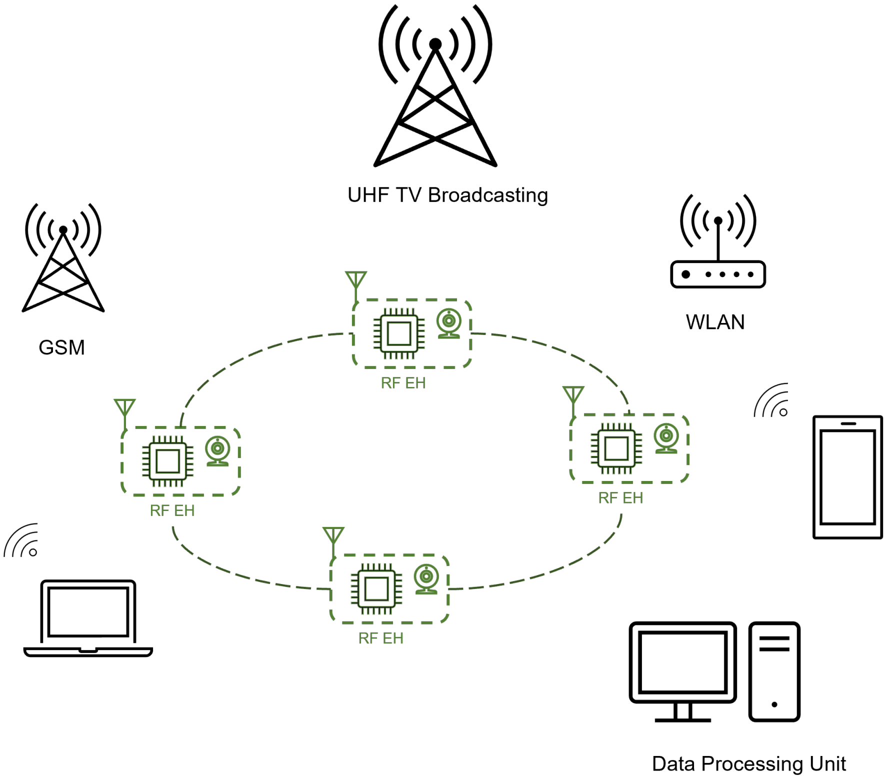

Figure 2.6: RF power sources.

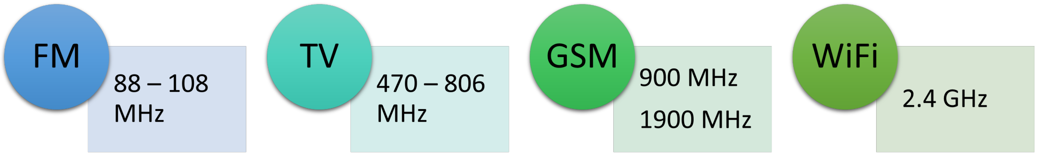

Figure 2.7: Frequency of RF sources [15].

that do not require any licence to transmit RF signals. Table 2.2 presents ISM band in ultra high frequency (UHF) spectrum.

The distance between the transmitter and the receiver plays an important role in the calculation of harvested power. Besides, signal strength, antenna gain and transmitted power also affect the received power. For a transmitter and a receiver in free space, the harvested power received by the receiving antenna can be calculated by the Friis transmission equation:

$$P_r = \frac{P_t G_t G_r \lambda^2}{(4\pi r)^2} \tag{2.6}$$

Where

- P_r and P_t are power at receiver and transmitter antenna respectively,

Table 2.2: ISM frequency bands in UHF spectrum [16].

Frequency	**Center Frequency**
433.05-434.92 MHz	433.92 MHz
902-928 MHz	915 MHz
2.4-2.5 GHz	2.45 GHz

- G_t is transmitter antenna gain,
- G_r is receiver antenna gain,
- λ is wavelength of transmitting RF wave and
- r is distance separating the antennas.

Another useful form of the Friis equation is given in terms of frequency:

$$P_r = \frac{P_t G_t G_r c^2}{(4\pi r f)^2} \tag{2.7}$$

Where

- c is speed of light and
- f is frequency of the RF wave.

2.3 Building Blocks of RF Energy Harvesting System

The building blocks of RF energy harvester is shown in Fig. 2.8. The receiving antenna receives the RF signal. The strength of the received signal decreases with the increasing distance between the transmitting and the receiving antennas. An impedance matching network maximizes the power transfer from the receiving antenna to the rectifier. Impedance matching network also provides passive amplification of the input voltage. The rectification circuit converts RF signal into a DC signal. The DC-DC converter produces a stable DC voltage that is further supplied to the load. The maximum power point tracking (MPPT) controller improves the performance of the converter.

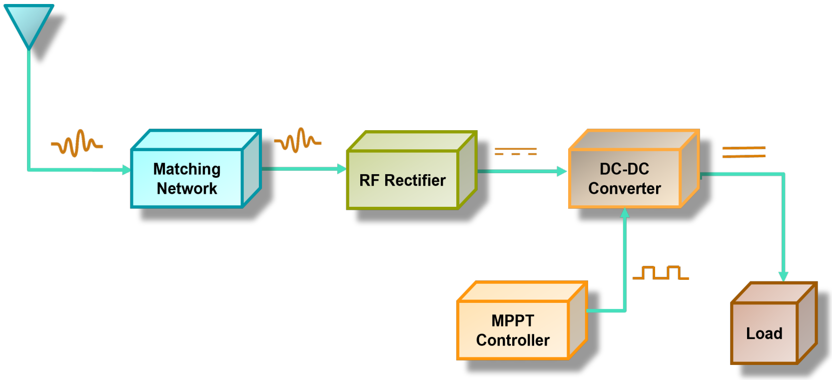

Figure 2.8: Building blocks of RF energy harvester

2.4 Matching Network Topologies

In an RF energy harvesting system, the main reason behind inefficiency is the power leakage during transmission of the signal from the receiving antenna end to the load. The matching network maximizes power transfer from antenna to load, considering the rectifier and the DC-DC converter as the load of the RF energy harvesting system. If there is any impedance mismatch, the incident wave will get reflected reducing the overall efficiency. The matching network matches the impedance and ensures maximum power transfer. Matching networks also work as low-pass filter and rejects higher order harmonics. Therefore, a matching network is a very important building block of the RF energy harvesting system.

In order to learn the approximate behavior of non-linear devices, they are usually designed by using small signal equivalent circuits [17]. RF signals are large input signals without any DC bias and therefore the rectifier operates in different regions of operation. Therefore the impedance of the rectifier varies with the variation of the input power and the load resulting in degradation of the PCE. Therefore the matching network needs to match impedance with for various input power levels and load impedance. Matching networks should have small form factor and wide bandwidth of operation. In order to achieve the desired impedance, tuning circuits can be used while second order matching circuit can be employed to improve the bandwidth[18]. However, if the order of the matching circuit is further increased, the bandwidth of the matching circuit decreases.

Lumped elements and microstrips are two most commonly used architectures of matching circuit. Lumped element based matching circuit have higher quality factor, Q and narrow bandwidth compared to distributed line. Lumped elements also have parasitic effects and therefore are not preferred for higher frequencies. T network, pi-network, shunt inductor, L-network are some common applications

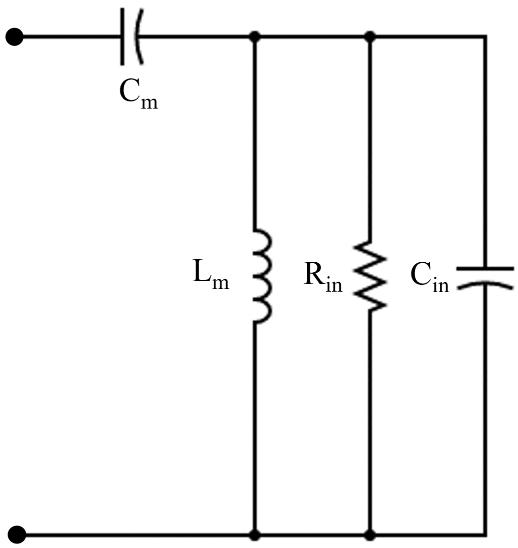

Figure 2.9: L matching network.

of lumped elements.

For low power input signals, L matching network is commonly used as it has minimal loss. Fig. 2.9 presents an L matching network circuit. The inductor in matching network preboosts the input signal of the rectifier. L matching network has higher quality factor, Q and thus suffers from lower bandwidth. The components of the matching network can be designed as follows:

$$R_s = R_{in}\frac{1}{1+Q^2} \tag{2.8}$$

Where

- R_s represents impedance of source,
- R_{in} represents input impedance of rectifier and
- Q represents quality factor.

Therefore, quality factor, Q can be obtained as:

$$Q = \sqrt{\frac{R_{in}}{R_s}} - 1 \tag{2.9}$$

Also quality factor, Q can determined from real and imaginary part of the impedance:

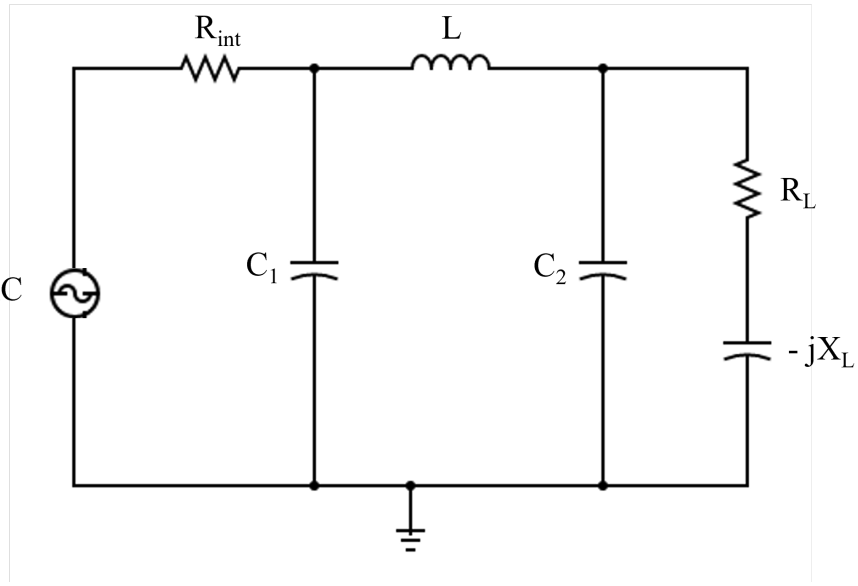

Figure 2.10: π matching network

$$Q = \frac{I_m(Z)}{R_e(Z)} = \frac{R_{in}}{\omega_0 L_m} - \omega_0 C_{in} R_{in} \tag{2.10}$$

The inductance of matching network can be determined by:

$$L_m = \frac{R_{in}}{\omega_0 (Q + \omega_0 C_{in} R_{in})} \tag{2.11}$$

The capacitance of matching network can be determined by:

$$C_m = \frac{R_{in}}{L_m (R_{in} - R_s)} \frac{1}{\omega_0^2 - \frac{1}{L_m C_m}} \tag{2.12}$$

In L matching network, there are only two components that can be tuned and therefore has less degree of freedom. This problem can be resolved by using π or T network. Fig. 2.10 presents a π network which can be designed using the following equation:

$$Z_{in} = [[(R_L - jX_L)||(\frac{1}{j\omega C_2})] + j\omega L]||(\frac{1}{j\omega C_1}) \tag{2.13}$$

2.5 Rectifier Topologies

In an RF energy harvesting system, the rectifier converts RF signal into DC signal. For RF energy harvesting system, input power in the receiving antenna end is low. Thus, RF to DC conversion efficiency needs to be high to design an efficient harvesting system. Various topologies have been adopted for designing an efficient RF-DC converter.

2.5.1 Diode Based Rectifier

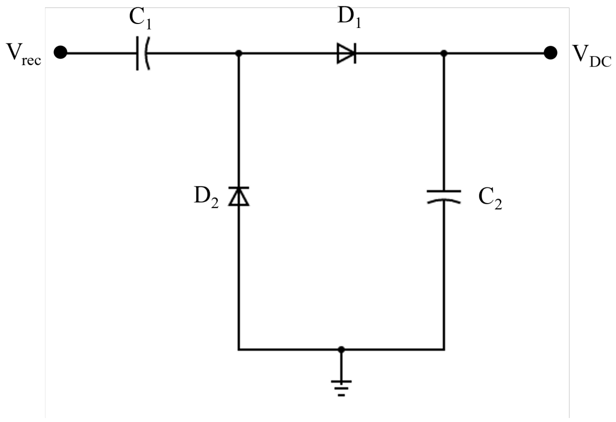

Figure 2.11: Voltage doubler circuit.

Voltage doubler is one of the most common architectures of RF rectifiers. Fig. 2.11 shows a voltage doubler circuit. Several stages of voltage doubler can be combined together to design CMOS diode connected RF rectifier. In the circuit, diode, D_1 and capacitor, C_2 form a rectifier while diode, D_2 and capacitor, C_1 form a voltage clamp. During the negative cycle of the input signal, D_2 is active and D_1 is in the off state. Current passes through D_2 and charges C_1 with the voltage V_{amp} - V_{th1}. During the positive cycle of the input signal, D_1 is active and D_2 is in the off state. Current passes through D_1 and charges C_2 with the voltage V_{amp} - V_{th2}. Therefore, the DC output voltage can be found as:

$$V_{out} = 2V_{amp} - V_{th1} - V_{th2} \tag{2.14}$$

Fig. 2.12 presents the circuit diagram of a Greinacher charge pump, also known as Villard multiplier. The circuit consists of CMOS diode-connected transistors and coupling capacitors to couple charge from the input signal to the transistors. For multistage Greinacher charge pump, the coupling capacitors needs to be larger to overcome the parasitics effect. To overcome this issue, Dickson charge pump architecture is implemented. Fig. 2.13 presents the circuit diagram of Dickson charge pump. In Dickson charge pump, input signal is coupled to the capacitor using parallel connection instead of series connection resulting in efficient voltage multiplication.

The major drawback of using CMOS diode-connected transistor based rectifier is the voltage

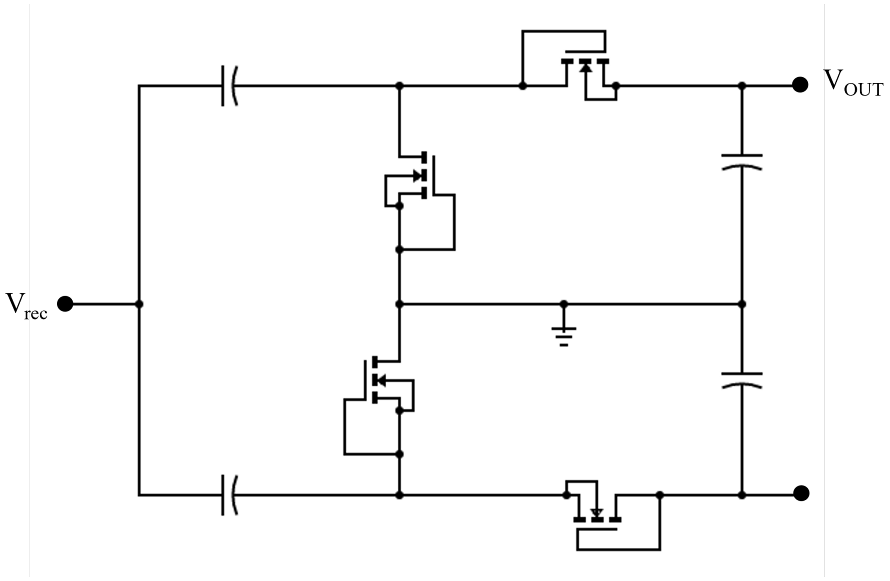

Figure 2.12: Greinacher charge pump.

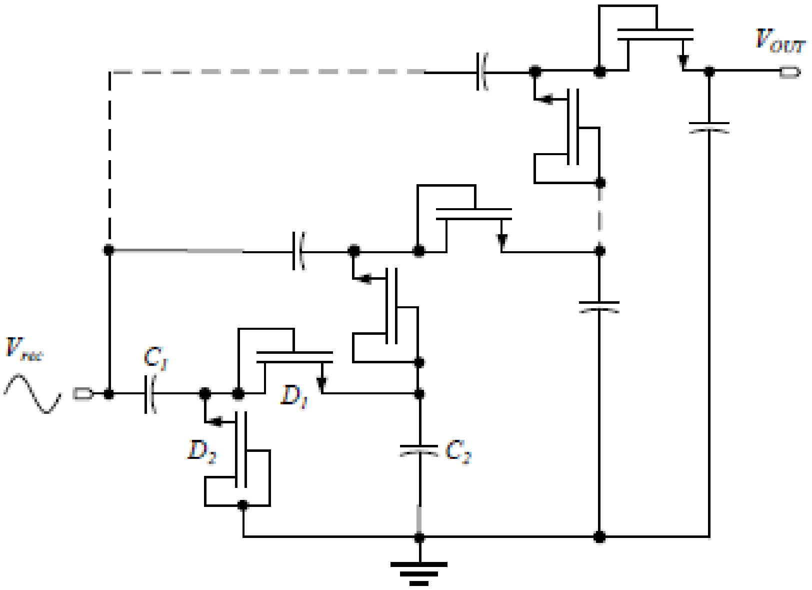

Figure 2.13: Dickson RF voltage multiplier.

drop across the transistors lowering the output voltage and hence the efficiency. Upon receiving an input voltage less than the threshold voltage, the rectifier will not even operate. Therefore, this type of architecture is not suitable for signals with low input voltage. If the input power is high, rectifying devices of high power capability such as Schottky diodes are preferred.

2.5.2 Cross Connected Differential Rectifier

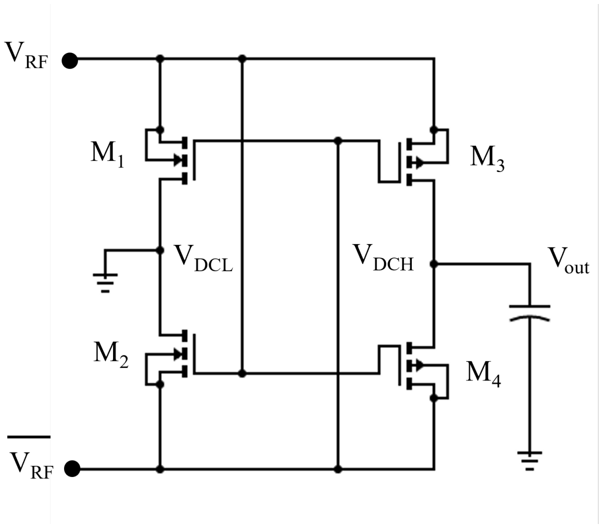

Figure 2.14: Cross-connected rectifier.

Fig. 2.14 shows a cross-connected differential rectifier architecture. In this architecture, differential RF signals are used instead of single-ended RF signal. The rectifier consists of both NMOS and PMOS transistors. The differential RF signals are used to operate NMOS and PMOS transistors making it a synchronous self-driven rectifier.

By cascading multiple stages together, the output voltage of the rectifier can be increased. Fig. 2.15 demonstrates the multistage cross-connected differential rectifier. While cascading multiple stages together, the differential input signals are applied parallel to to rectifying stages through coupling capacitors.

When the input voltage $\bar{V}_{rec}$ is high, current flows through the transistor, M_1 coupling the capacitor, C_{upper} and charges the first stage as $|V_{rec}|$- $(V_{Ndrop} + V_{Pdrop})/2$. Similarly, when the input voltage V_{rec} is high, current flows through the transistor, M_3 in the first stage and the transistor, M_2 in the second stage coupling the capacitor, C_{lower} and charges the second stage as $|V_{rec}|$- $(V_{Ndrop}$ $+ V_{Pdrop})/2$ and will be added charge stored in the first stage. Hence, with increasing number of stages, the output voltage of the rectifier is further increased.

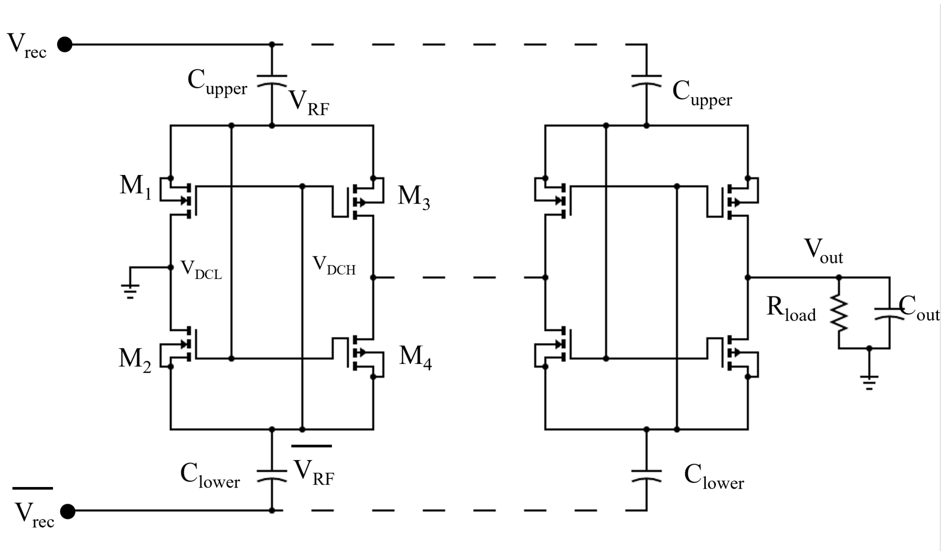

Figure 2.15: Multistage cross-connected differential rectifier.

2.5.3 Threshold Voltage Compensated Rectifier

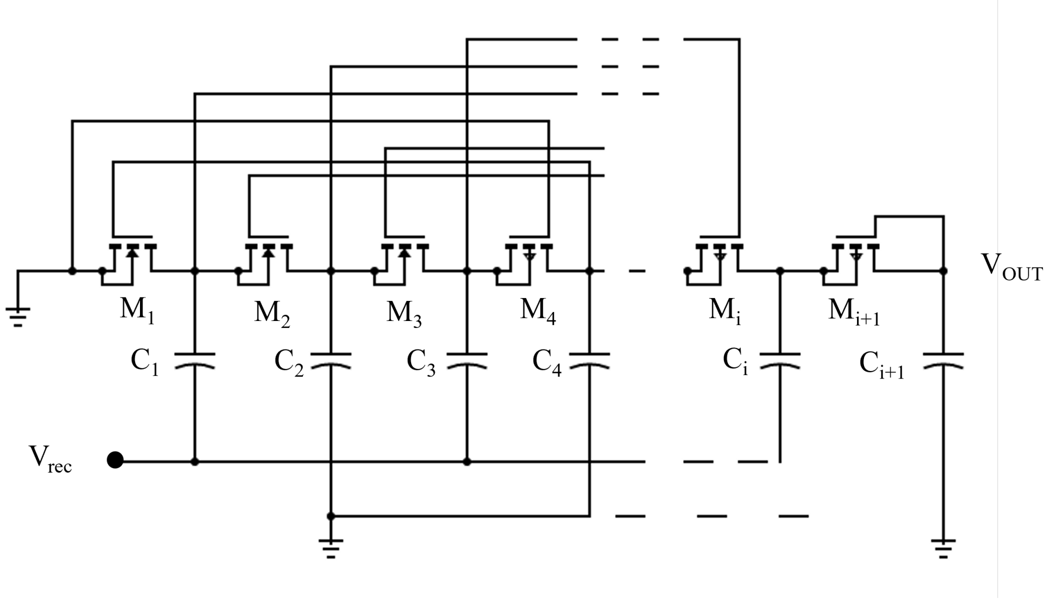

Figure 2.16: Three-levels threshold voltage compensation method.

From the discussion of subsection 2.5.2 it is clear that threshold voltage drop across diode-connected transistors results in lower output voltage and thus lower efficiency. The situation becomes critical when the amount of the input voltage is very low. Many active and passive techniques have been applied for the reduction of threshold voltage drop of the rectifier.

Fig. 2.16 presents a hybrid three-stage compensation rectifier. In this circuit, the gate of an

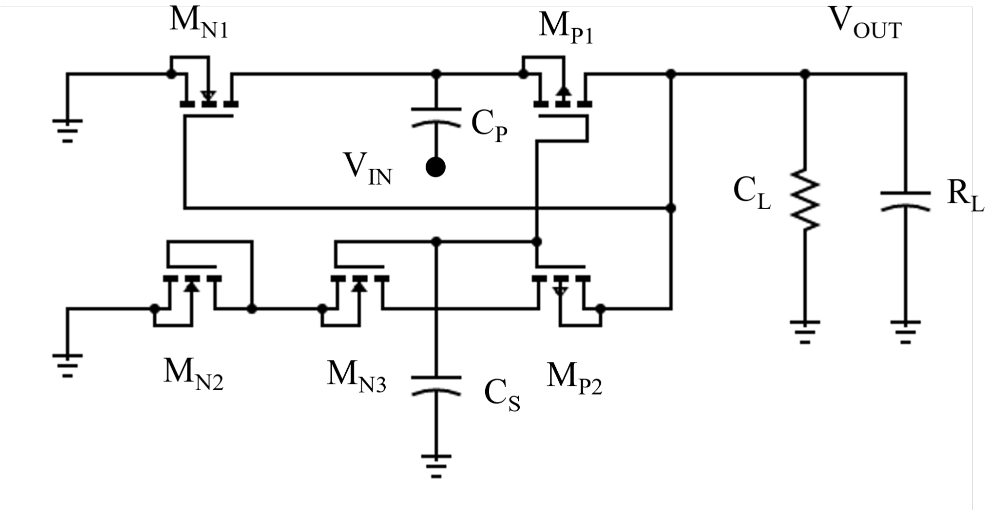

Figure 2.17: Rectifier with threshold voltage cancellation scheme[19].

NMOS transistor is connected to the source of the following NMOS transistor. Therefore, this structure provides a biasing gate to source voltage equivalent to the incremental voltage across each stage. In the case of PMOS transistors, gate is connected to the source of the last stage.

In this threshold voltage compensation technique, the gate-source voltage always contains DC component even during reversed bias condition. Therefore, the power loss due to leakage current will also increase. Thus there needs to be a trade-off between the number of stages of the rectifier and its leakage power loss.

Fig. 2.17 presents circuit architecture of the rectifier using threshold voltage cancellation scheme. Utilizing both positive and negative cycles of the input signal along with the output voltage, the rectifier cancels the threshold voltage effect. The rectifier consists of M_{P1} and M_{N1} transistors. The threshold voltage of the transistor, M_{P1} is compensated by rest of the circuit components. The threshold voltage of the transistor, M_{N1} is compensated by the output voltage, V_{OUT} of the rectifier. The output voltage, V_{OUT} is obtained by:

$$V_{OUT} = 2V_{IN} - V_{dMN1} \tag{2.15}$$

Where

- V_{dMN1} represents voltage drop across transistor M_{N1} and
- V_{IN} represents input voltage.

By using these threshold compensation schemes, the RF energy harvesting system for very low input voltage can be designed. However, additional power is also required to operate the auxiliary circuits. Therefore, while designing the RF rectifier, the circuit should be designed with minimal internal power loss.

2.6 DC-DC Converter

Generally, DC-DC converters are used to convert one voltage level of direct current (DC) source into a different level of voltage so that the proper voltage can be obtained to power up the electrical and electronic systems [20]. The DC-DC converters are capable of providing regulated voltage with high efficiency. DC-DC converter can be of various types such as boost, buck, and buck-boost [21]. If a system requires higher voltage than the source voltage, then boost converter is used. On the other hand, if a system requires lower input voltage then the buck converter is used. Fig. 2.18 shows the schematic diagram of a typical DC-DC boost converter.

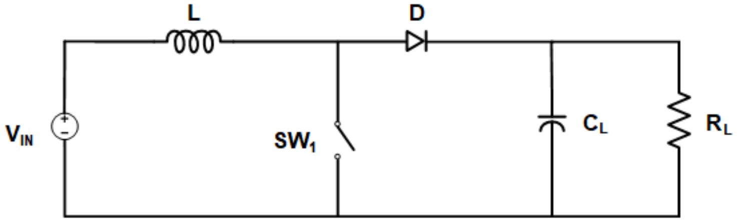

Figure 2.18: Schematic diagram of a typical DC-DC boost converter.

The operation mode of a DC-DC converter can be divided into two categories: (a) continuous conduction mode (CCM), and (b) discontinuous conduction mode (DCM). In CCM, the inductor current during a switching cycle is always greater than zero. On the other hand, in DCM the inductor current during a switching cycle hits zero level [22].

Fig. 2.19 (a) shows the CCM and Fig. 2.19 (b) shows DCM operation of a DC-DC converter. In the figures, t_1 and t_2 represent the on time of the NMOS and the PMOS switches, respectively. The input impedance and the output voltage conversion ratio depend on the average inductor current.

The typical advantage of a CCM operation of DC-DC converter is summarized below:

- The voltage gain is function of duty cycle
- The input current is continuous
- The ripple component of the inductor current is lower than the average current of other components

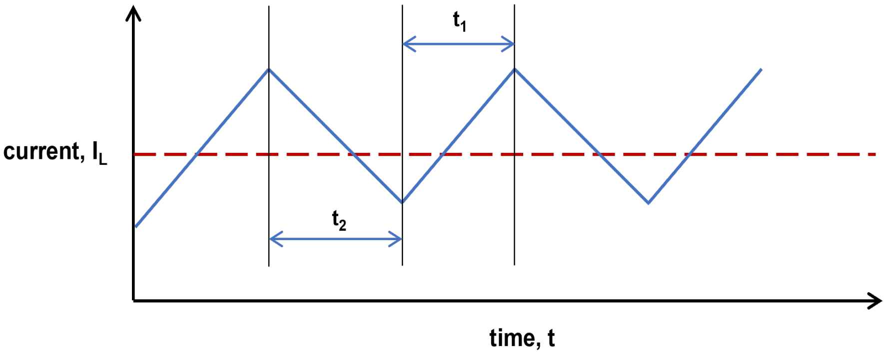

(a) CCM operation

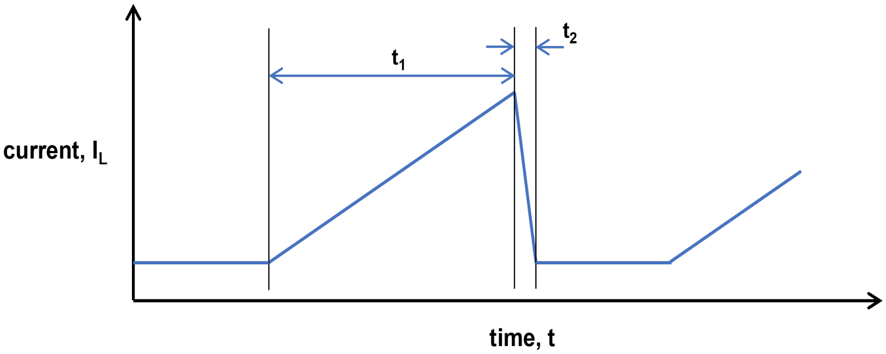

(b) DCM operation

Figure 2.19: Inductor current waveform

- Higher efficiency can be achieved compared to a DCM mode of operation

The major drawback of CCM operation is that the efficiency in light load is very low since the inductor current is always greater than zero, . The advantages of DCM operation are:

- The voltage gain is function of load as well as frequency
- An inductor component size usually smaller than a CCM mode
- At light load, the efficiency is higher than a CCM mode of operation

Besides if the input power is low, the DC-DC boost converters provide higher efficiency if they are operated in DCM.

The peak inductor current, I_{L_peak} can be obtained by using following equation:

$$I_{L\_peak} = \frac{t_1}{L} \tag{2.16}$$

The average inductor current, I_{L_avg} can be found by using the following equation:

$$I_{L\_avg} = \frac{V_{IN} t_1 (t_1 + t_2) f_s}{2L} \tag{2.17}$$

Where

- V_{IN} represents input voltage of DC-DC converter,
- t_1 represents rising time,
- t_2 represents falling time,
- f_s represents switching frequency of the converter,
- L represents inductance.

The input impedance of a DC-DC converter can be expressed as follows:

$$\frac{V_{IN}}{I_{L\_avg}} = \frac{2L}{t_1^2 f_s}(1 + \frac{t_2}{t_1})^{-1} \tag{2.18}$$

If the boosting ratio is very high this equation can be simplified as:

$$\frac{V_{IN}}{I_{L\_avg}} = \frac{2L}{t_1^2 f_s} \tag{2.19}$$

From the equation, it can be concluded that the input impedance of the converter depends on inductance, switching frequency as well as NMOS switch on time. For a boost converter with fixed switching frequency, an increase of the NMOS on time, t_1 will result in decreased impedance of the converter. On the other hand, an increase in the inductance will increase the impedance of the converter.

Since the available input power of the proposed RF energy harvesting circuit is very small and is limited by the available RF transmittable power as well as the distance between a transmitter and a receiver, a DCM mode of operation is chosen in this design due to the reasons explained above.

2.7 MPPT Controller

Unlike mechanical or thermal energy, RF energy has very low power density resulting in low received power for harvesting purpose. Therefore, efficient power management system needs to be integrated with the RF energy harvesting system to increase its efficiency. The RF energy harvesting system can operate at a maximum power point (MPP) for a particular input power that allows the maximum energy transfer from the source to the load. A change in the available input power results in a change in MPP and thus the output power will also be changed. If the system operates at any operating point other than the maximum power point, the output power delivered to the load will be lowered. To overcome this issue, maximum power point tracking (MPPT) technique can be implemented. MPPT is a technique that tracks the MPP of a system by matching the impedance between the source and the load.

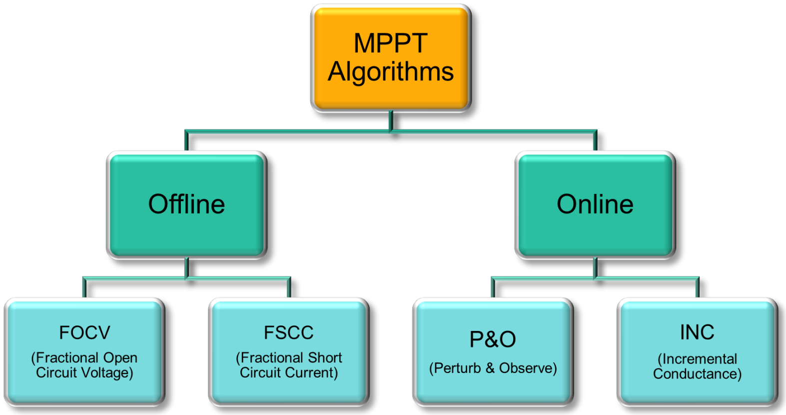

Figure 2.20: Classification of MPPT algorithms.

Various MPPT algorithms have been implemented in literature to design energy harvesting systems. Fig. 2.20 shows the major classifications of MPPT algorthm: offline and online [23]. In the case of online algorithm: perturb and observe (P&O) or incremental conductance (INC), true maximum power point at a particular instant is tracked but is difficult to implement and has low convergence speed [24]. Alternatively, offline algorithm such as fractional open circuit voltage (FOCV) or fractional short circuit current (FSCC) uses an approximation of the maximum power point and thus is easier to implement [25]. However, under the condition of rapidly varying input power, the conventional MPPT algorithms suffer from poor tracking speed [23]. This issue can be resolved by implementing artificial intelligence based algorithms such as neural network (NN) and fuzzy logic controller (FLC) [26].

Chapter 3

PROPOSED RADIO FREQUENCY ENERGY HARVESTING SYSTEM

3.1 Radio Frequency Based Energy Harvesting

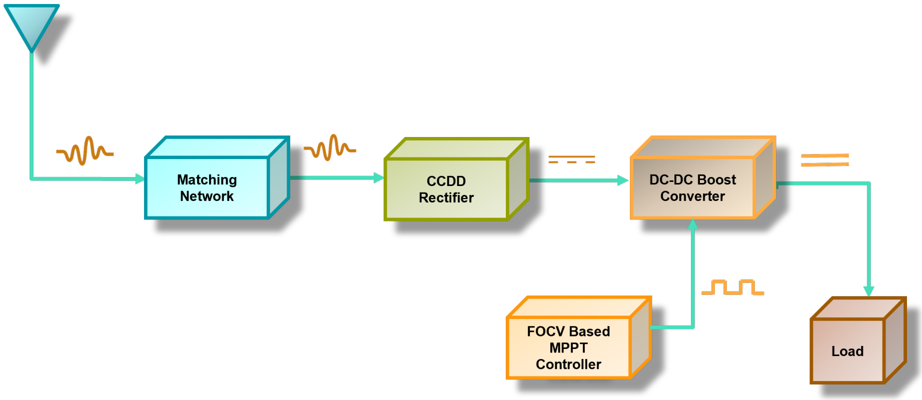

Figure 3.1: Block level diagram of the proposed RF energy harvester

The overall block diagram of the proposed RF energy harvester is shown in Fig. 3.1. The ambient RF signals of specific frequency are received by an antenna in the receiver side. An active rectifier has been added to convert the RF signal into a DC signal. The matching network in the system matches the impedance between the antenna and the rectifier. A DC-DC boost converter has been added to the system to obtain stable DC voltage at the output. In order to extract the maximum available power, an MPPT controller has also been incorporated in the system.

3.2 Antenna Model

Generally, radio frequency signals are received in the form of sinusoidal wave. In order to properly utilize this power rectification operation of the signal is imperative. Therefore, design of a rectifier is a crucial part of the overall design of the RF energy harvesting system.

Before discussing the design of the rectifier, it is important to address the role of antenna . In a radio frequency-based energy harvesting system, an antenna works as a transducer that converts the radio frequency signal into an electrical signal. Therefore, choosing or designing an appropriate antenna is a crucial part of RF energy harvesting system design. For a transmitter and a receiver in the free space, the harvested power received by the receiving antenna can be calculated by the Friis transmission equation:

$$P_r = \frac{P_t G_t G_r \lambda^2}{(4\pi r)^2} \tag{3.1}$$

where,

- P_r refers to received power,
- P_t refers to transmitted power,
- G_t refers to transmitter antenna gain,
- G_r refers to receiver antenna gain,
- λ refers to wavelength of transmitted RF wave,
- r refers to distance separating the antennas.

From equation (3.1), it can be observed that the distance between the transmitter and the receiver plays a very significant role in the calculation of the power received by the receiving antenna. Additionally, the received power also depends on the signal strength, antenna gain and transmitted power.

Another useful form of the Friis equation is given in terms of frequency:

$$P_r = \frac{P_t G_t G_r c^2}{(4\pi r f)^2} \tag{3.2}$$

where c is speed of light and f is frequency of RF wave.

In the case of radio frequency signal transmission, effective isotropic radiation power (EIRP) is an important term:

$$P_{EIRP} = P_t G_t \tag{3.3}$$

EIRP indicates the transmission power at which an isotropic emitter would have to be supplied in order to generate a defined radiation power at distance r. An antenna with gain G_t, can be operated with transmission power, P_t where P_t is lower than P_{EIRP}/G_t. According to the U.S. Federal Communications Commission (FCC) regulations, the P_{EIRP} is 4W for the frequency range from 300 MHz to 1.5 GHz.

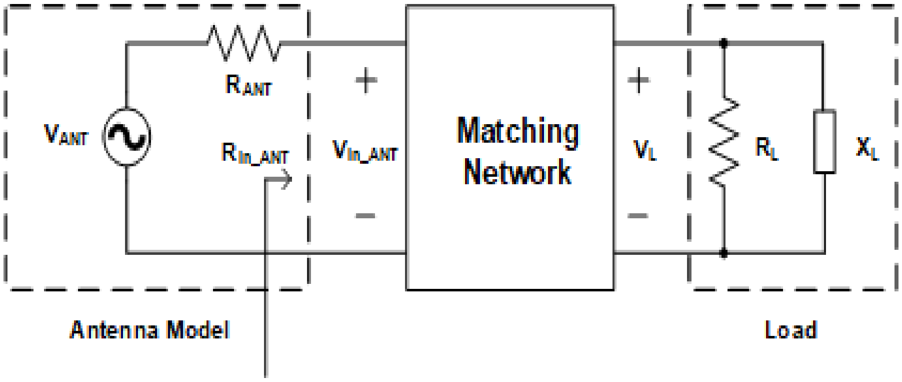

Figure 3.2: Equivalent antenna model

Fig. 3.2 presents an equivalent model of the receiving antenna. In the figure, R_{ANT} is the internal resistance of the antenna.

$$R_{ANT} = R_{rad} + R_{loss} \tag{3.4}$$

Where R_{rad} is the radiation resistance of the antenna and R_{loss} is the loss resistance of the antenna.

Antenna radiation resistance, R_{rad} represents the power radiation by the antenna into the free space and is a property of the shape and the dimension of the antenna. Antenna loss resistance, R_{loss} is the ohmic resistance of the antenna. Power received by the antenna can be expressed as:

$$P_{ANT} = \frac{V_{ANT}^2}{8R_{ANT}} \tag{3.5}$$

Therefore, the voltage received in the antenna end can be estimated from the power received at the antenna end:

$$V_{ANT} = 2\sqrt[2]{2V_{ANT}P_{ANT}} \tag{3.6}$$

Where

- P_{ANT} refers to power received from antenna,
- R_{ANT} refers to series resistance loss and
- V_{ANT} refers to sinusoidal voltage source.

In order to convert the AC signal into a DC signal various rectification schemes are used. These widely applied schemes are not applicable for high frequency signals as the received power is very low resulting in low voltage in the receiving antenna end. This low voltage in the receiving antenna end is inadequate to operate the CMOS rectifier circuit.

3.3 Matching Network

The power collected from the receiver antenna can be modelled as an AC sinusoidal voltage source V_{ANT} with a lossy series resistance R_{ANT}. From equation (3.6), it can be observed that the voltage generated by the antenna is proportional to the square root of the power received by the antenna. Therefore, if the power received by the antenna is reduced, the voltage obtained from the antenna is also decreased. According to [27], if the input RF power is below -6 dBm, the peak voltage that can be obtained from the antenna is 0.158 V which is too low to operate the rectifier.

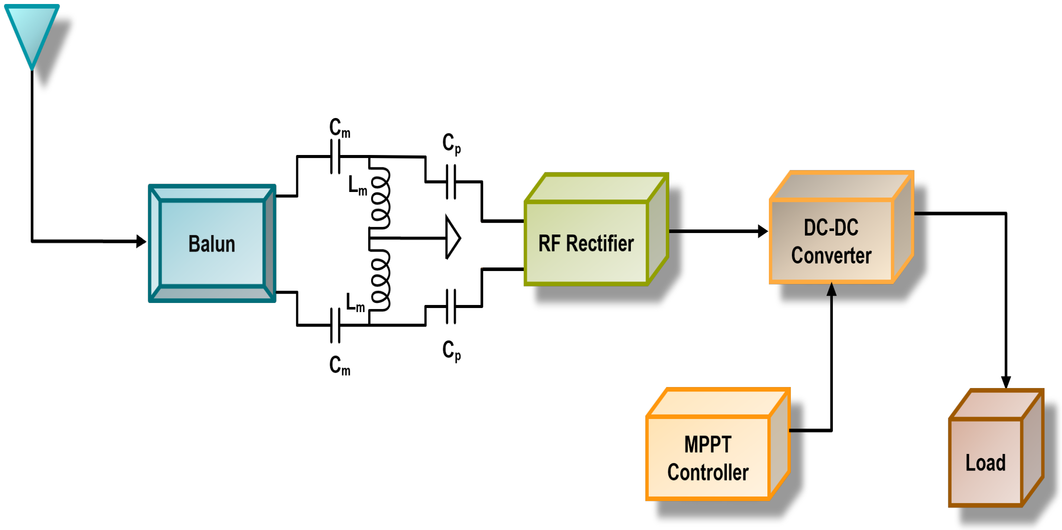

Figure 3.3: Complete front end of RF energy harvesting system

On the other hand, the minimum power required to operate the rectifier successfully can be expressed as:

$$P_{ANT} = (\frac{R_{ANT} + R_{real\_RECT}}{R_{imag\_RECT}})^2 (\frac{V_{in\_RECT}^2}{8R_{ANT}}) \tag{3.7}$$

Where

- R_{ANT} refers to the sum of the internal losses of the antenna,
- R_{real_RECT} refers to the real part of the input impedance of the RF rectifier and
- R_{imag_RECT} refers to the imaginary part of the input impedance of the RF rectifier.

From equation (3.7) it can be observed that the minimum power required from the antenna depends upon the input impedance of the RF rectifier. In order to operate the rectifier with an input power lower than -6 dBm, the real and the imaginary parts of the impendance of the rectifier can be adjusted to achieve proper power, P_{ANT} which in return will provide adequate voltage, V_{ANT}. Therefore, an impedance matching network is considered as one of the major components of the design of the RF energy harvester.

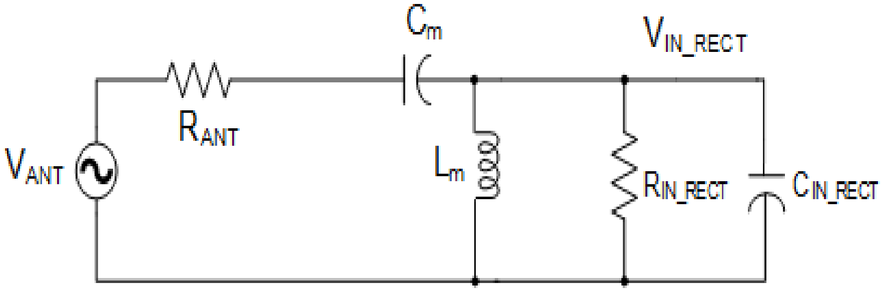

Figure 3.4: Matching network of the proposed energy harvester

A matching network has been introduced to the system to obtain the power required for operating the rectifier. The complete circuit diagram of the front-end of the proposed RF energy harvester along with the proposed matching network is shown in Fig. 3.3. Fig. 3.4 shows the circuit diagram of the proposed L-matching network. As the power received from the antenna is very low, it is imperative to reduce the losses due to the impedance mismatch between the output of the antenna and input of the rectifier. The proposed matching network matches the impedance between them and minimize the losses due to impedance mismatch. Besides, it boosts the voltage obtained from the antenna to an adequate level so that the RF rectifier can operate successfully using the available voltage.

In the design, L-matching network has been proposed due to its simplicity and ease of tuning. The values of C_m and L_m can be calculated by using the following expressions [28], [29]:

$$C_m = \frac{1}{\omega_r R_{ANT}} \sqrt[2]{\frac{R_{ANT}}{R_{IN} - R_{ANT}}} \tag{3.8}$$

$$L_m = \frac{R_{IN}}{\omega_r R_{ANT} C_{IN} + \frac{1}{\sqrt[2]{\frac{R_{ANT}}{R_{IN} - R_{ANT}}}}} \tag{3.9}$$

Where

- R_{IN} is the input resistance of the rectifier,
- C_{IN} is the input capacitance of the rectifier and
- ω_r is the resonant frequency.

The voltage gain obtained from the matching network can be expressed as:

$$Gain = \frac{V_{IN-RECT}}{V_{ANT}} = \frac{1}{2} \sqrt[2]{\frac{R_{IN}}{R_{ANT}}} \tag{3.10}$$

From equation (3.10), it can be observed that the voltage of the antenna can be boosted by using the matching network if the input resistance of the rectifier, R_{IN} is greater than the output resistance of the antenna, R_{ANT}. In order to calculate proper values of C_m and L_m, the following procedure was followed:

- Select the value required to operate the rectifier, $V_{IN-RECT}$.
- Calculate the value of the gain to obtian the desired value of $V_{IN-RECT}$ from equation (3.10).
- Select an arbitrary value of R_{ANT}.
- Calculate the value of R_{IN} from equation (3.10).
- By using given values of Cin and ω_r , proper values of C_m and L_m can be obtained from equation (3.8) and (3.9).

After following the above steps, the values obtained for C_m and L_m are 550 fF and 45 nH, respectively. Besides, the value of the input capacitance was fixed to 45 nF.

Fig. 3.5 presents the transient response of the RF front end. Fig. 3.5 (a) shows the voltage received from the receiving antenna. From the figure it can be observed that the voltage received is

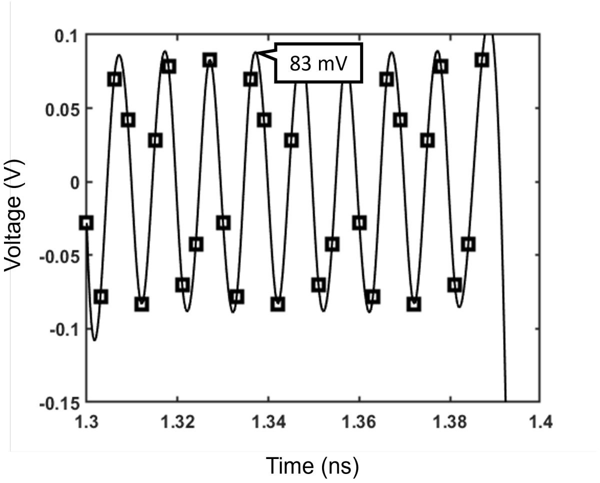

(a) P_{IN}

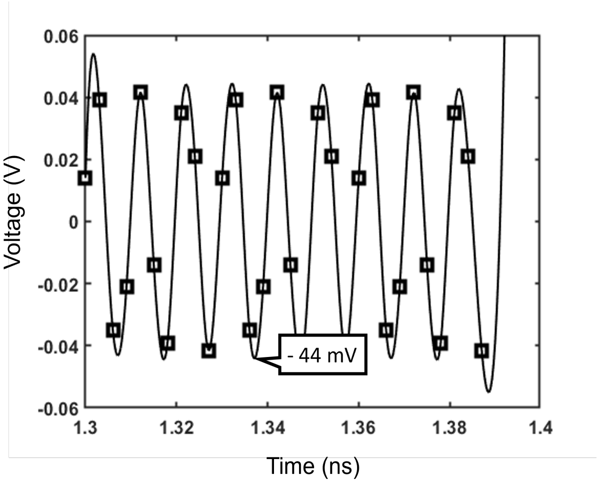

(b) RF_N_IN1

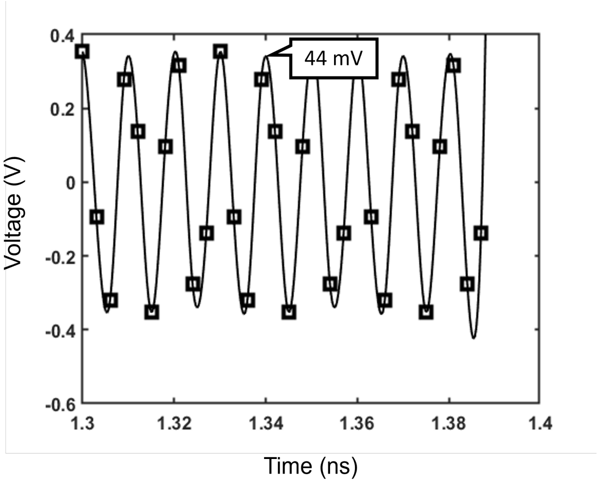

(c) RF_P_IN1

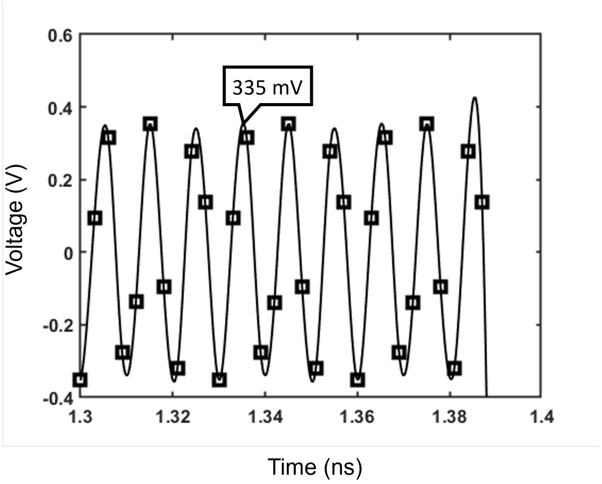

(d) RF_N1

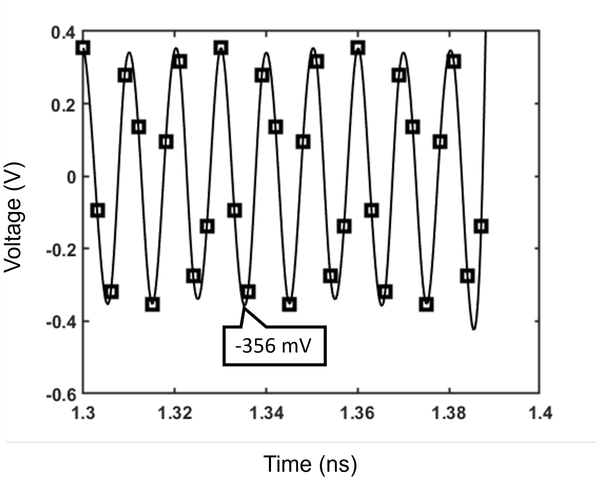

(e) RF_P1

Figure 3.5: Voltages of the RF front end at -10 dBm input power.

in the form of a sinusoidal wave with an amplitude of 83 mV. An ideal balun with 1.3 dB loss has been added to the system in order to convert single-ended signal into a differential one. Fig. 3.5 (b) and Fig. 3.5 (c) present the output signal of the balun. From Fig. 3.5 (b) and Fig. 3.5 (c) it can be observed that the balun produces two differential signals, RF_N_IN1 and RF_P_IN1 with the amplitude of 44 mV. The output of the balun is then fed into the matching network. Fig. 3.5 (d) and 3.5 (e) present the output signals of the matching network. The proposed matching network produces two differential signals, RF_N1 and RF_P1 with an amplitude of 335 mV. Therefore, it can be concluded that the matching network is able to boost the voltage by approximately 7.6 times.

3.4 RF Rectifier

3.4.1 Design of Cross-Coupled Differential Drive Rectifier

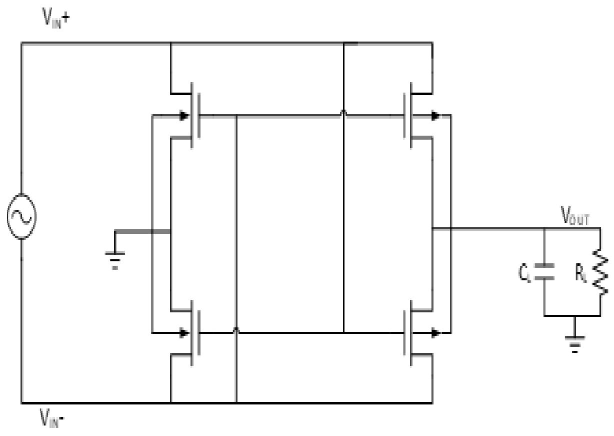

Figure 3.6: Schematic diagram of a typical cross-connected active rectifier.

Generally, the RF signal received from the antenna is an AC signal. As electronic devices require DC power to operate, an AC-to-DC converter is required so that the collected power can be utilized to power the subsequent blocks. As the power received from the antenna is very low, the power conversion efficiency of the rectifier needs to be high so that adequate output power is available.

Cross-connected CMOS rectifier structure in Fig. 3.6 is one of the most commonly used topologies due to its low-voltage requirement [30]. If the input voltage of the rectifier increases, the voltage conversion ratio also improves significantly. However, the amount of leakage current also increases with the increase in the input power because both NMOS and PMOS transistors are simultaneously on during the transition period. In order to obtain better sensitivity, the size of the transistors can be increased which will result in higher parasitic capacitance. Besides, increased transistor size will cause more reverse-current to flow which limits the efficiency at higher input power. Therefore, the cross-connected rectifiers are able to provide high PCE for a limited input power range. On the other hand, if the sizes of the transistors are too small, the on resistance of the transistors, R_{on} will increase. Hence, the conduction loss of the circuit will increase which will lower the available output voltage, V_{RECT} of the rectifier. Therefore, the sizes of the transistors need to be chosen carefully.

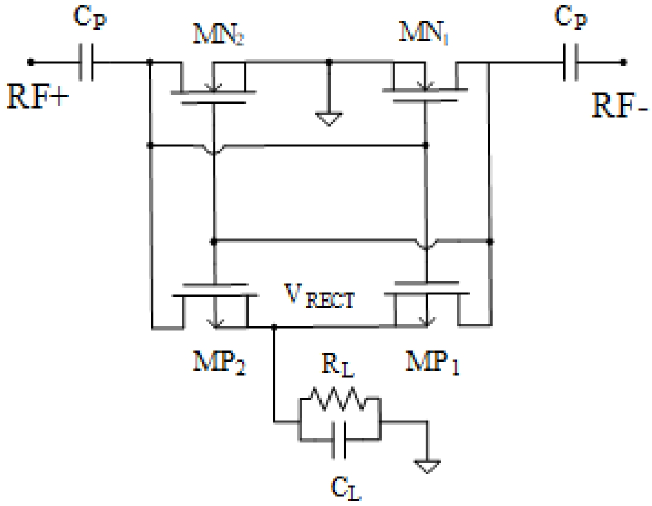

Figure 3.7: Schematic diagram of the proposed active rectifier.

A cross-connected rectifier shown in Fig. 3.7 has been proposed in the system in order to obtain high power conversion efficiency (PCE) with limited available input power ranges. To ensure the operation of the rectifier with low available input voltage, transistors with low threshold voltage have been chosen.

After careful trial and error simulations, the sizes of the NMOS and PMOS transistors were selected. Transistors MP_1 and MN_2 are on during the discharging phase and transistors MP_2 and MN_1 are on during the charging phase. The schematic diagram of the half-cycle circuit is provided in Fig. 3.8. Fig. 3.9 (a) and 3.9 (b) present the charging and the discharging phases in each RF input cycle.

To obtain the output voltage of the active rectifier, KVL can be applied in Fig. 3.8. After applying KVL in Fig. Fig. 3.9 (a) and 3.9 (b), we get equations (3.11) and (3.12) respectively:

$$V_{cp} = -V_{RF-IN} + V_{dn} - V_{DC} \tag{3.11}$$

$$V_{cp} = -V_{RF-IN} + V_L + V_{dp} \tag{3.12}$$

Table 3.1: Transistor sizes of the proposed RF rectifier

Transistors	**Size(μm)**	**Number of Fingers**
PMOS	30/0.18	25
NMOS	30/0.18	20

From equations (3.11) and (3.12) we get the following:

$$V_L = -2V_{RF-IN} + V_{DC} - (V_{dn} + V_{dp}) \tag{3.13}$$

As the output voltage of the rectifier is collected across its load, it can be represented as:

$$V_{RECT} = 2V_{RF-IN} + V_{DC} - (V_{dn} - V_{dp}) \tag{3.14}$$

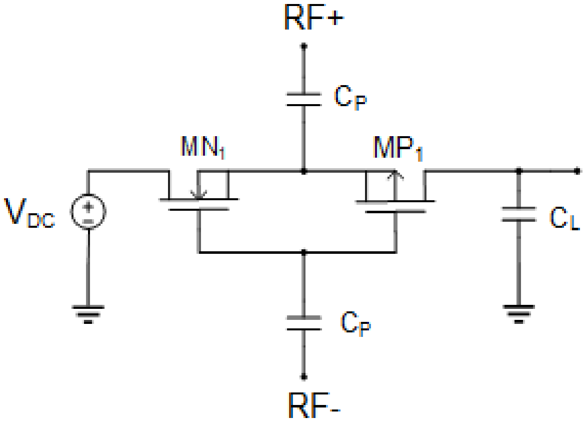

Figure 3.8: Half-cycle schematic of the proposed RF rectifier.

From equation (3.14) it can be observed that the output voltage of the rectifier, V_{RECT} is twice that of the input voltage, R_{RF-IN}. Besides, equation (3.14) shows that if the voltages V_{dn} and V_{dp} are reduced, the value of the output voltage of the rectifier, V_{RECT} can be increased.

3.4.2 Simulation Results of RF Rectifier

The circuit was simulated at 900 MHz RF input frequency with 1.5 dB loss of a balun. The proposed front-end of the RF energy harvester was designed using standard 180 nm CMOS process. Fig. 3.10 demonstrates the transient response of the input (RF+ and RF-) and the output voltages of the

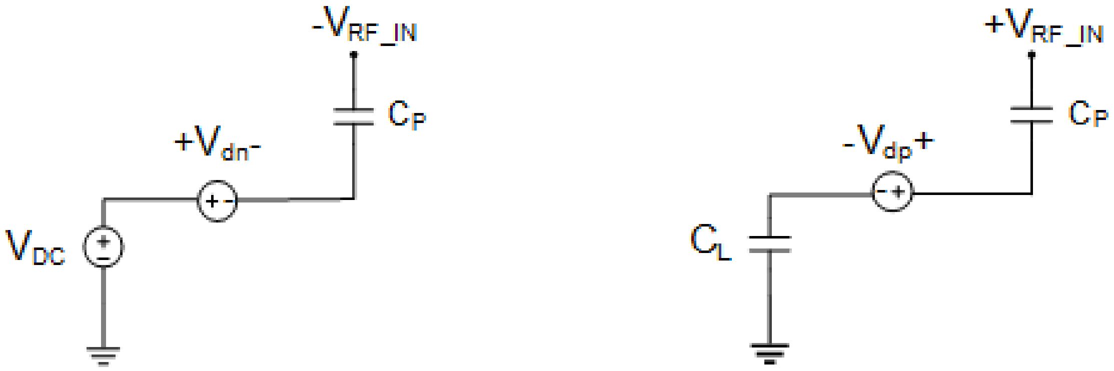

(a) Charging phase

(b) Discharging phase

Figure 3.9: Half-cycle voltage operation.

proposed rectifier. From the figure it can be observed that for -10 dBm input power the input (peak) of the rectifier RF+ and RF- are 560 mV, respectively. For a 3.4 k Ω load, a DC voltage of 0.46 V can be obtained for -10 dBm input power.

Fig. 3.11 demonstrates the efficiency of the rectifier with respect to various load impedances for different input powers. From the figure, it can be observed that the efficiency of the rectifier changes with the variation of the input power. Additionally it can be found that that the efficiency of the rectifier changes with the changes in the load impedance. For -10 dBm input power shown in Fig. 3.11 (a) it can be observed that with the increment of the load resistance the efficiency of the rectifier increases. For -10 dBm input power, the rectifier provides highest efficiency of 66.59% at 5 kΩ load impedance. Besides it can be observed that the rectifier operates above 60% efficiency for the load impedance range 3 kΩ - 5 kΩ. On the other hand, at 0 dBm input power the rectifier operates with 57% efficiency with 1.6 kΩ load impedance. The rectifier operates with the lowest efficiency of 33.44% with 5 kΩ load impedance. Therefore, it is crucial to find the optimal load impedance so that the rectifier operates with proper efficiency for the input power range -10 dBm to 0 dBm. After carefully observing the performance of the rectifier for various load impedances for the input power range -10 dBm to 0 dBm, 3.45 kΩ load impedance chosen to be optimal.

Fig. 3.12 shows the output voltage, V_{RECT} for various input powers, P_{IN} and for various conditions of the load, R_L of the proposed rectifier. With the increment of the input power, the output voltage of the rectifier increases. Also, with the increment of load resistance, the output voltage of the rectifier increases. The proposed rectifier provides the maximum output voltage of 0.96 V for 3.6 kΩ resistive load at 0 dBm input power. The rectifier produces minimum output voltage of 0.416 V for 3 kΩ resistive load at -10 dBm input power.

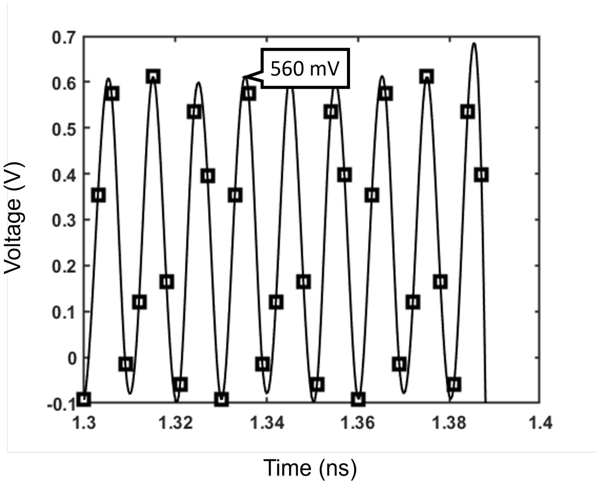

(a) RF+

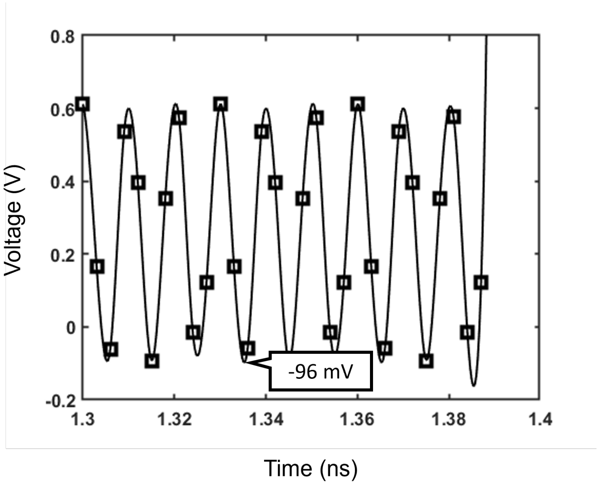

(b) RF-

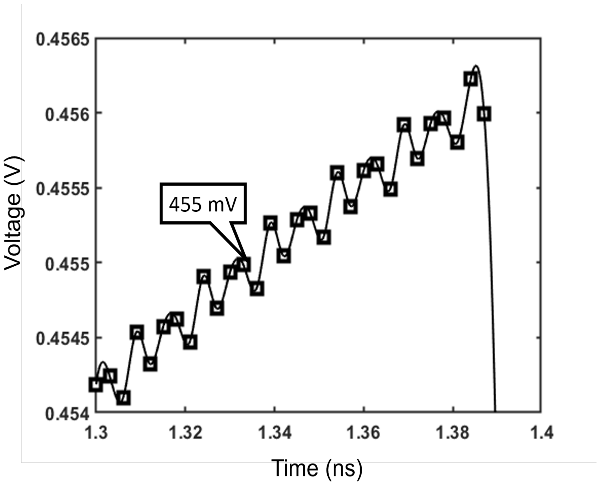

(c) Vrect

Figure 3.10: Voltages of the RF rectifier at -10 dBm input power.

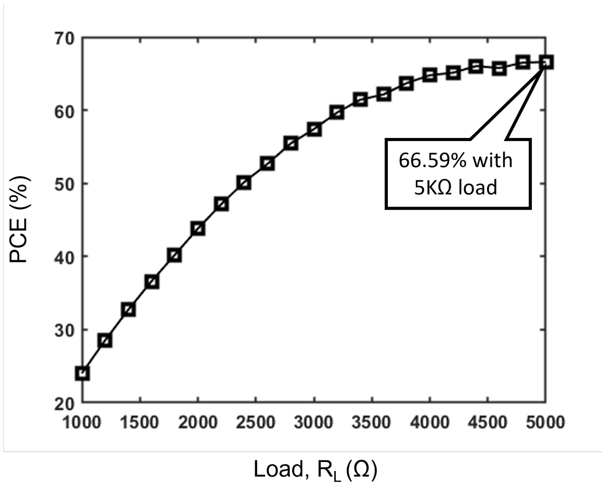

(a) Efficiency at -10 dBm

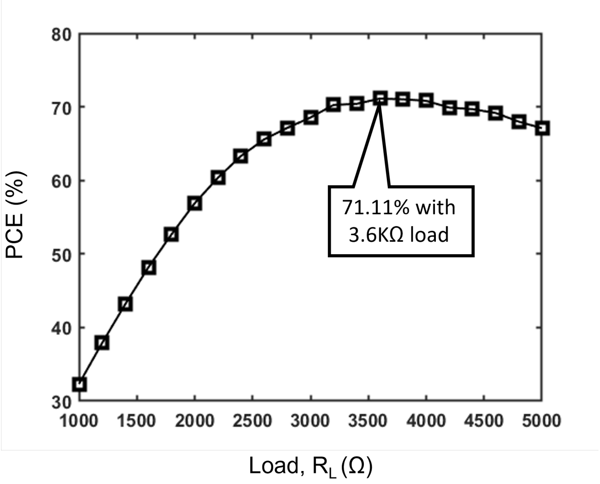

(b) Efficiency at -8 dBm

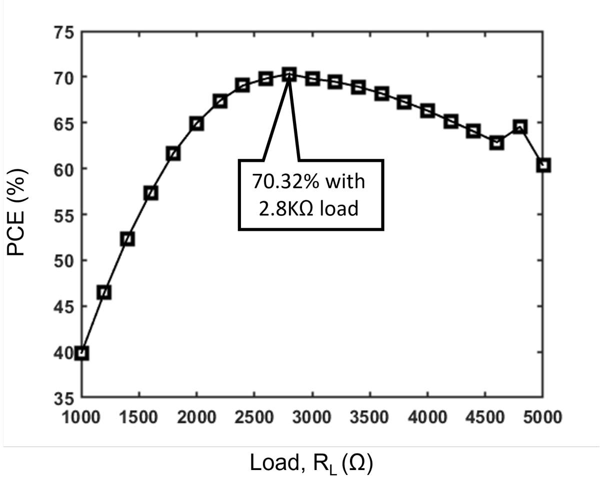

(c) Efficiency at -6 dBm

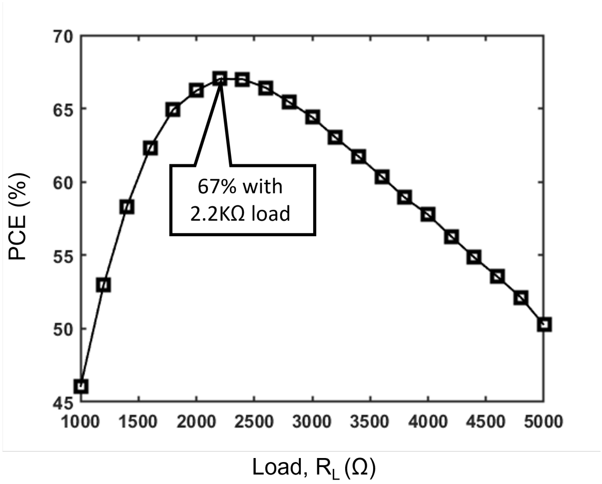

(d) Efficiency at -4 dBm

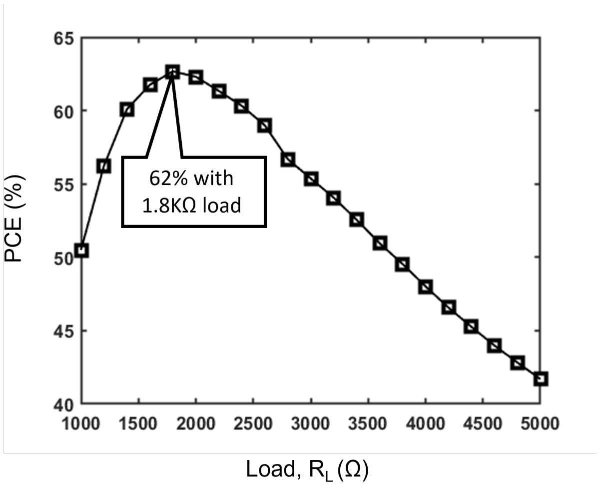

(e) Efficiency at -2 dBm

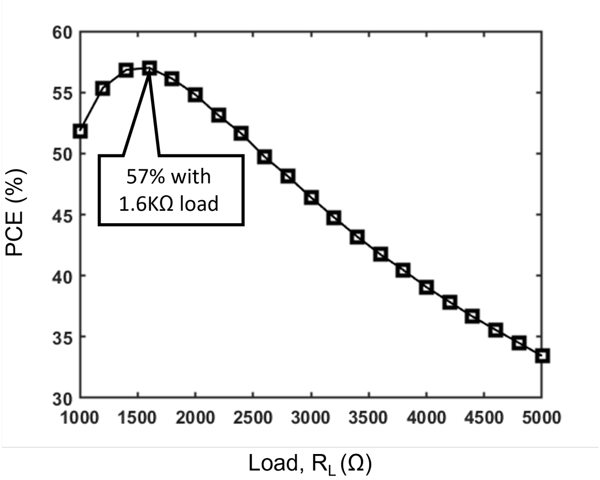

(f) Efficiency at 0 dBm

Figure 3.11: Efficiency of the proposed rectifier with various input power, P_{IN} and load conditions, R_L.

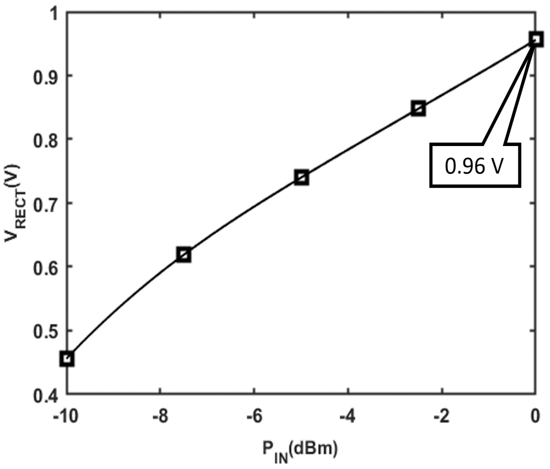

(a) V_{RECT} at with 3.6 kΩ load impedance

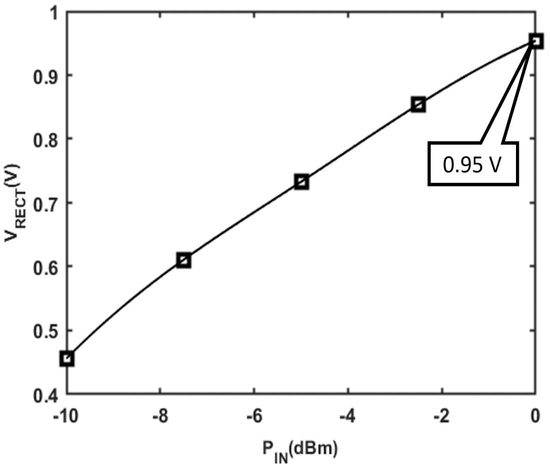

(b) V_{RECT} at with 3.45 kΩ load impedance

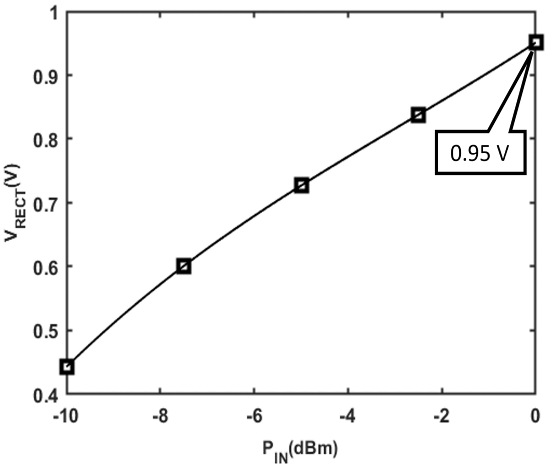

(c) V_{RECT} at with 3.3 kΩ load impedance

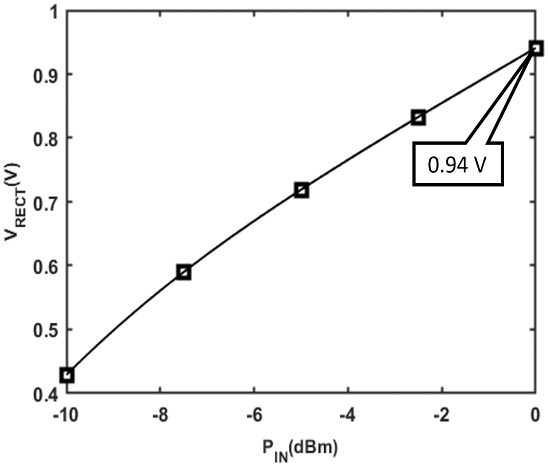

(d) V_{RECT} at with 3.15 kΩ load impedance

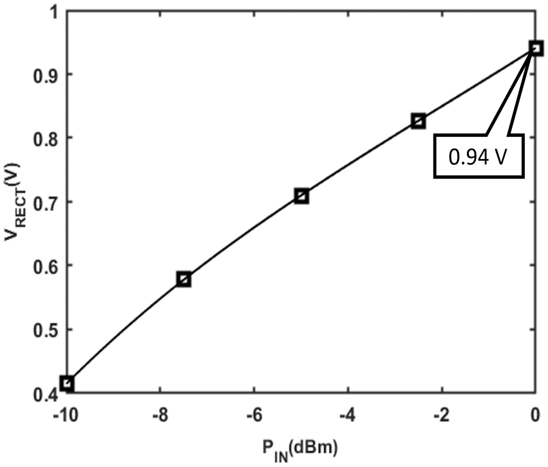

(e) V_{RECT} at with 3 kΩ load impedance

Figure 3.12: Rectifier's output voltage, V_{RECT} vs. input power, P_{IN} for various load impedances, R_L

Table 3.2: Summary of simulated load vs. efficiency of RF rectifier

P_{IN} **(dBm)**	R_L **(kΩ) Range**	$V_{RECT}(V)$ **Range**	**Efficiency Range (%)**
-10	3.4 - 5.5	0.46 - 0.58	66.59 - 61
-8	2.2 - 5.0	0.49 - 0.73	71.11 - 60.35
-6	1.8 - 5.0	0.53 - 0.87	70.32 - 60.31
-4	1.4 - 3.8	0.57 - 0.94	67.01 - 58.31
-2	1.2 - 3.8	0.65 - 1.1	62.67 - 49.54
0	1.0 - 3.6	0.72 - 1.2	57 - 41.75

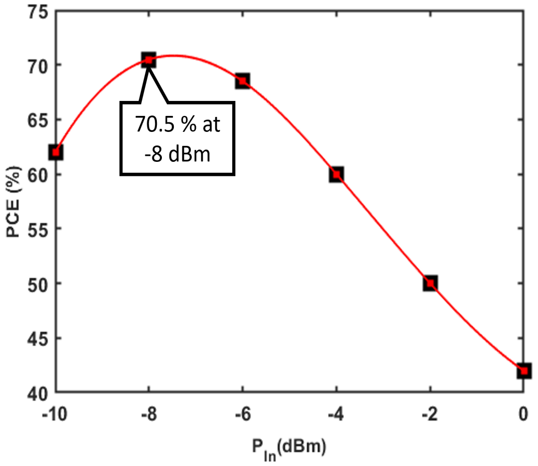

Figure 3.13: PCE of the proposed RF rectifier with respect to various input power, P_{IN}.

Fig. 3.13 showcases the PCE of the proposed rectifier for various RF input power with 3.6 kΩ. At -10 dBm input power, the rectifier operates with 62% efficiency. The rectifier performs with the maximum efficiency of 70.5% at -8 dBm input power. From the figure it can be observed that with the increment of the input power, the efficiency of the rectifier is decreased. The rectifier operates with the lowest efficiency of 42% at 0 dBm input power. As the proposed rectifier was designed using cross-connected topology, the shoot-through current will be increased with the increment of the input power resulting in lower efficiency. While designing an RF rectifier, choosing the proper MOSFET is crucial. If the input power of the RF energy harvesting system is low, the voltage available from the receiving antenna will be low. If voltage applied to the rectifier is very low, it cannot operate the rectifier. Therefore, low-threshold MOSFET switches have been applied to design the rectifier which

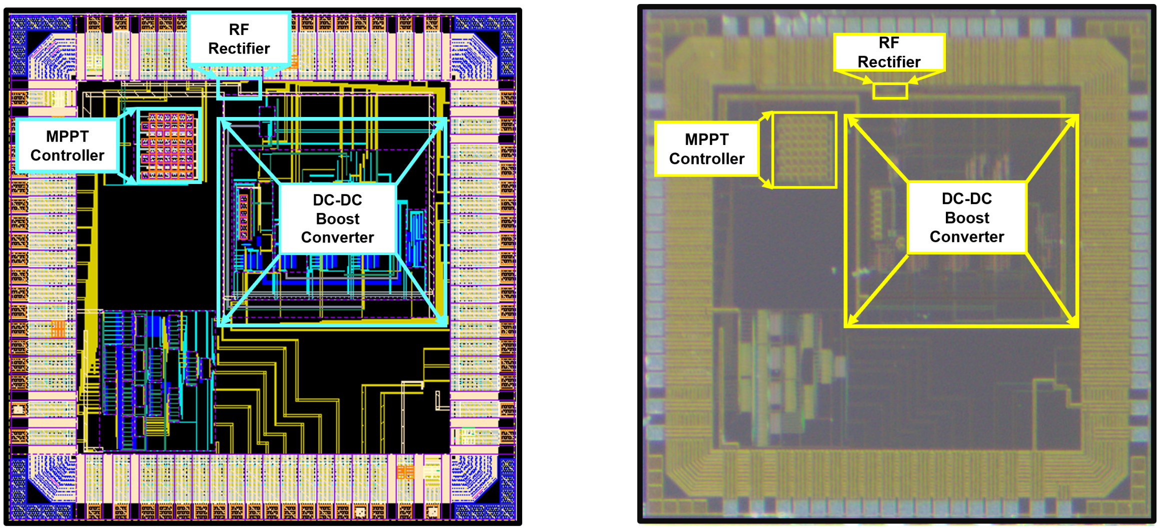

(a) Layout

(b) Chip Micro-photograph

Figure 3.14: Layout and chip micro-photograph of implemented RF energy harvesting system.

also resulted in additional leakage current to the device. Due to this leakage current, the PCE of rectifier decreases with the increased input power.

The performance of the rectifier for various load impedances, R_L has been summarized in table 3.2.

3.4.3 Measurement Results of RF Rectifier

Fig. 3.14 presents the layout and the chip micro-photograph of the implemented RF energy harvesting system which has been realized in a standard 180 nm CMOS process. Fig. 3.15 demonstrates the test circuit of the proposed RF energy harvesting system.

Fig. 3.16 shows the layout and the chip micro-photograph of the implemented RF rectifier component of the proposed system. The area of the rectifier is 59 μm x 17 μm. As the rectifier operates in ultra high frequency range of 895 MHz to 920 MHz, the DC-DC converter part has been separated from the rectifier part so that the high frequency signal does not affect the circuits associated with the DC-DC converter. Fig. 3.17 shows the test circuit of the RF rectifier that consists of an RF signal generator, an attenuator, a power splitter and the proposed RF energy harvester.

The RF signal is being generated from Adafruit Feather MO with SX137 LoRa based RF signal generator. The control unit of Feather Mo is an ATSAMD21G18 ARM Cortex MO processor, clocked at 48 MHz and at 3.3V logic. Following are some specifications of the Feather MO:

- ATSAMD21G18 @ 48 MHz with 3.3V logic/power,

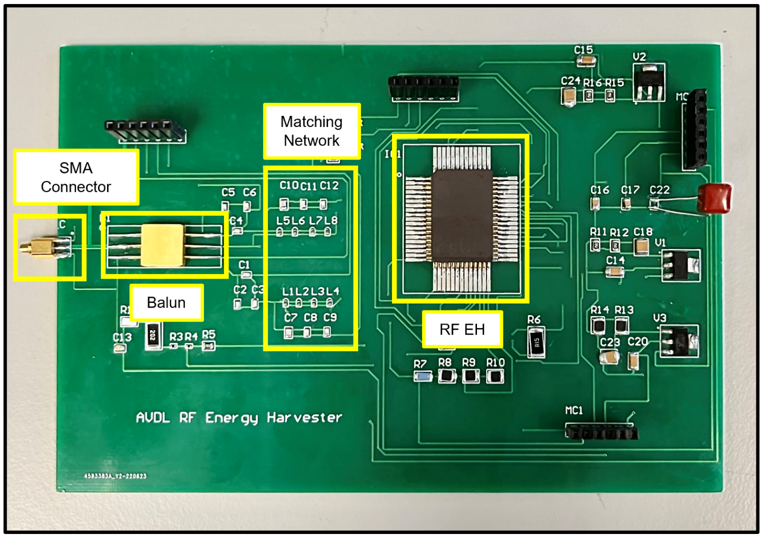

Figure 3.15: Test Circuit

- 3.3V regulator with 500 mA peak current output,
- USV native support, comes with USB bootloader and serial port debugging,
- Packet radio with native ready-to-go Arduino libraries,
- Uses the license-free ISM bands (ITU ”America” @900 MHz),
- Simple wire antenna or spot for uFL connector,
- +5 dBm to +20 dBm upto 100 mW power output capability,

The Feather MO is capable of generating power ranging from +5 dBm to +20 dBm. As the proposed RF energy harvesting system has been designed to operate from -10 dBm to 0 dBm input power range, a 15 dB attenuator is used to attain the power level appropriate for the proposed system. A power splitter has been also used to measure the input impedance of the rectifier. Finally, the signal is being transmitted to the proposed energy harvesting system via a 1-to-1 type balun. The balun is single-to-differential ended with 50 Ω input and output impedances. The measured value of the input impedance through the balun is 43 − 116j.

Fig. 3.18 shows the input and the output voltages of the proposed RF rectifier. For the input voltage of 330 mV, the rectifier is producing an output of 670 mV. Therefore, it can be concluded that the rectifier is working as expected.

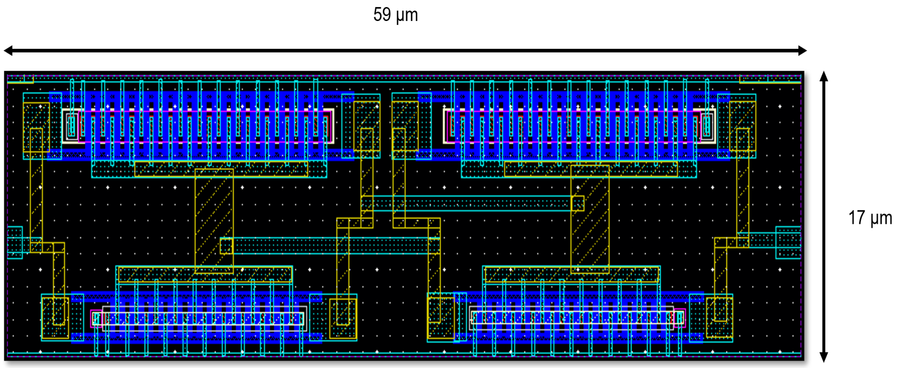

(a) Layout

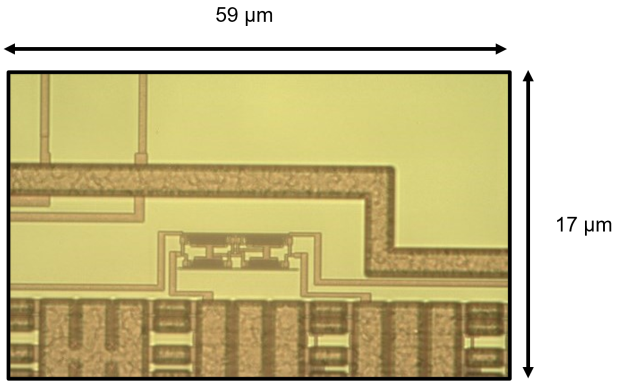

(b) Chip Micro-photograph

Figure 3.16: Layout and micro-photograph of the proposed RF rectifier.

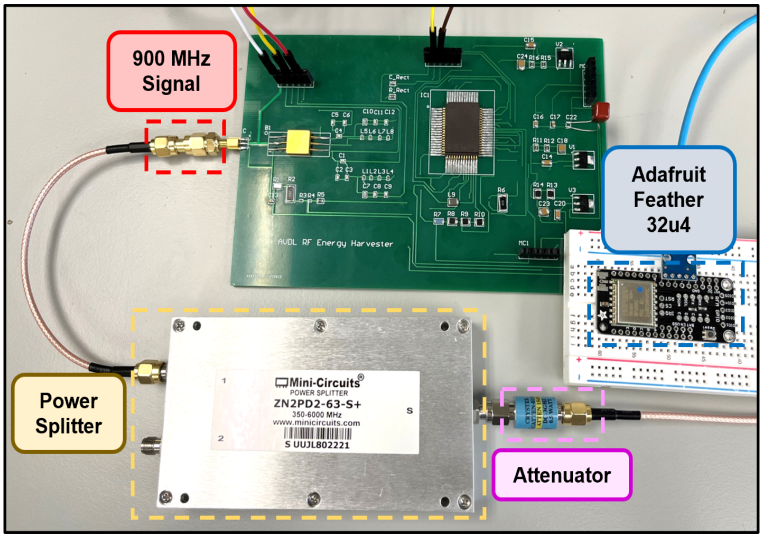

Figure 3.17: Test circuit of RF rectifier

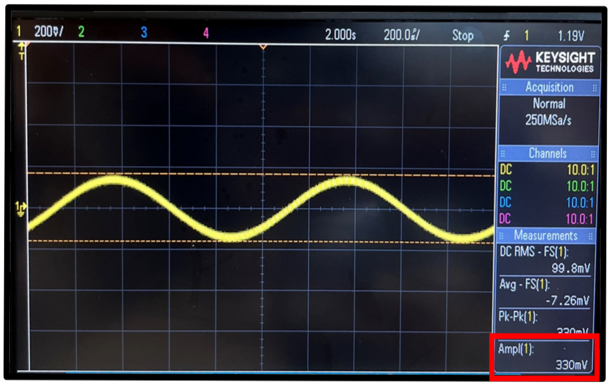

(a) Input voltage

(b) Output Voltage

Figure 3.18: Rectifier's input and output voltage.

3.5 DC-DC Boost Converter

3.5.1 Design of DC-DC Boost Converter

For the proposed RF energy harvester, a DC-DC boost converter has been designed in order to boost the available low input voltage from the antenna so that it can be used to power up the electronic circuits. Typically, the antenna output voltage is too low to be directly used as a voltage source to power subsequent blocks of the system. Besides, the obtained voltage is not regulated. Hence, a boost converter can be used to boost up the input voltage up to usable voltage level as well as a regulated output voltage of the system. Fig. 3.19 shows the schematic diagram of the synchronous DC-DC boost converter.

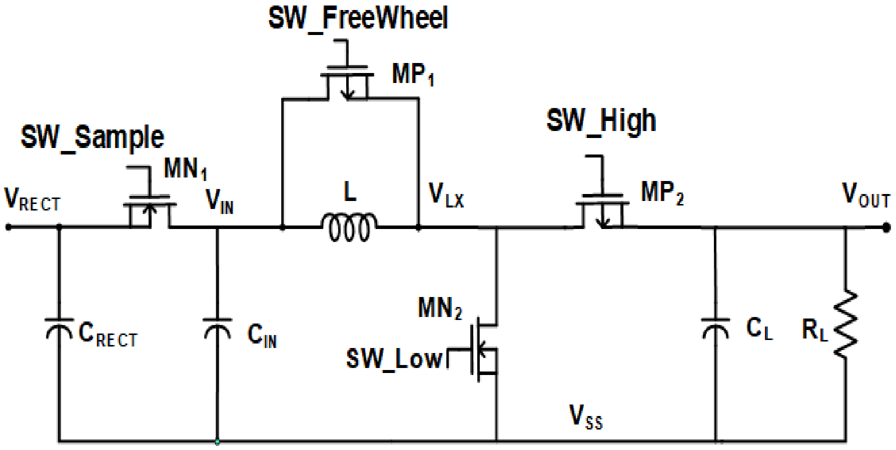

Figure 3.19: Schematic diagram of boost converter.

The DC-DC boost converter is has four switches:

- an NMOS low side switch, MN_2,
- a PMOS high side switch, MP_2,
- an inductor free-wheeling current switch, MP_1, and
- a sample and hold switch, MN_1.

The proposed converter is a synchronous DC-DC boost converter. The low side switch, MN_2 charges the inductor and PMOS high side switch, MP_2 discharges the inductor. MOS transistors have been used as low side and high side switches due to their lower threshold voltages compared to the conventional diodes. Besides, the on resistance R_{on} of the MOS transistors can be adjusted by varying its size and thus the power loss due to R_{on} is lower compared to the traditional converters.

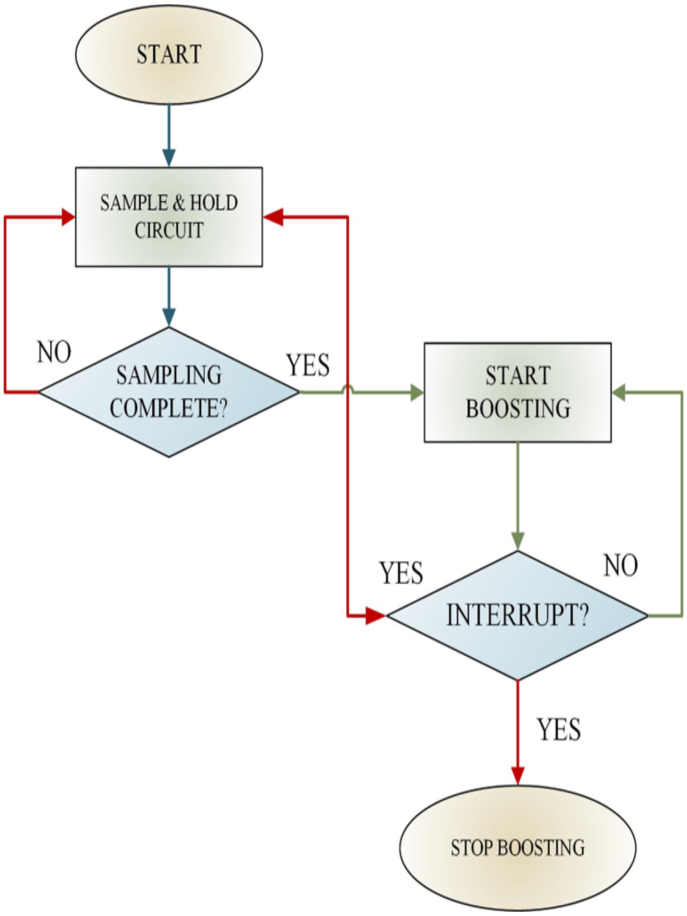

Figure 3.20: Operation of the proposed boost converter.

Fig. 3.20 demonstrates the operation of the proposed boost converter. The reference voltage of a converter helps to determine its duty cycle. For the proposed case, the reference voltage of the converter is collected from outside. By using a sample and hold (S&H) circuit, the open circuit output voltage of the rectifier is collected and stored. Sampling and boosting are two alternative operating modes of the converter. During the sampling operation MN_1, MN_2 and MP_2 falls into off-state and vice versa for boosting mode.

Inverted oscillator signal (OSCB) is connected to the sample and hold switch of the converter. Therefore, whenever the sampling operation is complete, the boosting operation begins. If there is any interruption, the boosting operation stops, and the converter stats operating in the sampling mode. The protection function of the converter can be implemented externally. The internal protection bit is set low by default. Upon detection of the protection signal, boosting operation stops.

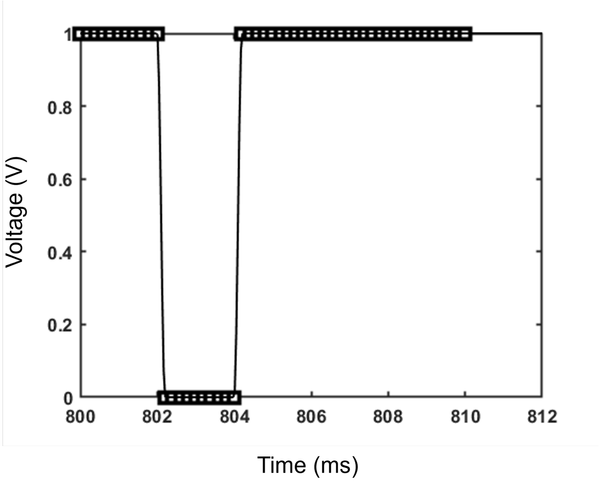

(a) OSCB

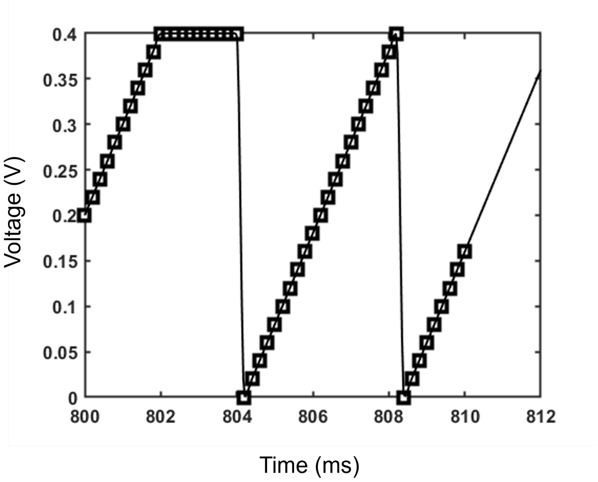

(b) V_IN

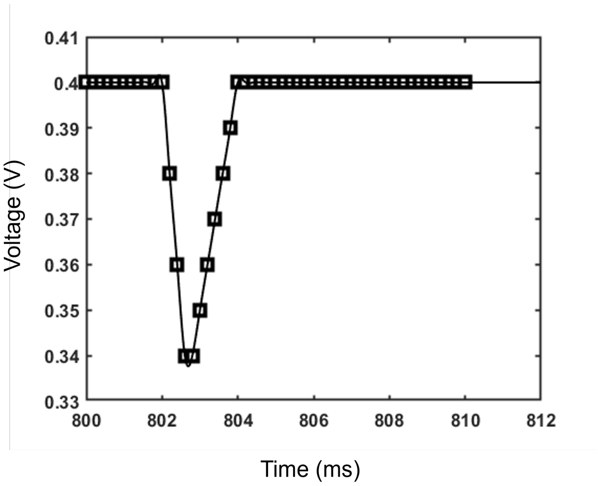

(c) OUT_Sample

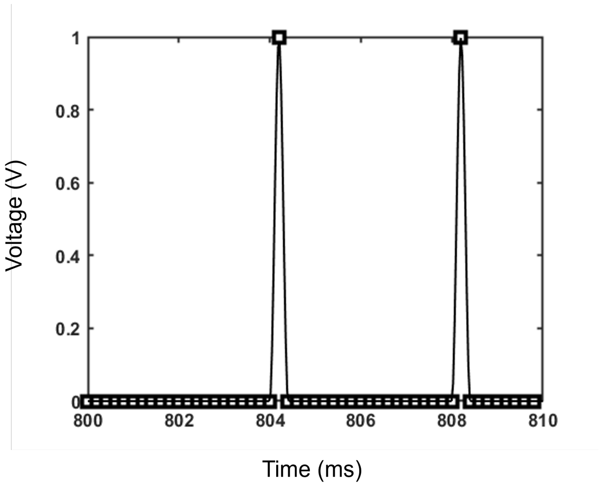

(d) SW_NMOS

Figure 3.21: Low-side switch control waveforms.

3.5.2 Simulation Results of DC-DC Boost Converter

Fig. 3.21 presents simulation waveform of low-side control signal. As mentioned in Section 3.5.1, the DC-DC boost converter is operated in sampling or boosting operating mode. From Fig. 3.21 it can be observed that when the signal OSCB (3.21(a)) is high, the DC-DC converter is operating in the boosting mode and otherwise in the sampling mode for low OSCB. Therefore, all other operations of the DC-DC boost converter are halted.

Fig. 3.22 shows the simulation waveform of the high-side switch control signal. Using an EN_DEL signal instead of large hysteresis comparator voltage allows to eliminate fault comparator signal during the operation of a low-side switching circuit. The EN_DEL signal provides adequate delay time for the ZCDB signal. From the figure it can be observed that when the inductance node voltage, V_{LX} is greater than the output voltage, V_{OUT} the PMOS switch is on and the DC-DC converter produces a DC output voltage, V_{OUT} of 1.08 V.

Fig. 3.23 presents the simulated efficiency of the overall RF energy harvesting system for various input power levels.

3.5.3 Measurement Results of DC-DC Boost Converter

Fig. 3.24 presents (a) the layout and (b)the chip micro-photograph of boost converter. The area of the boost converter is 917 μm x 728 μm. In order to avoid interference between the DC signal and the ultra high frequency signal, the input of the DC-DC boost converter is fed from an equivalent

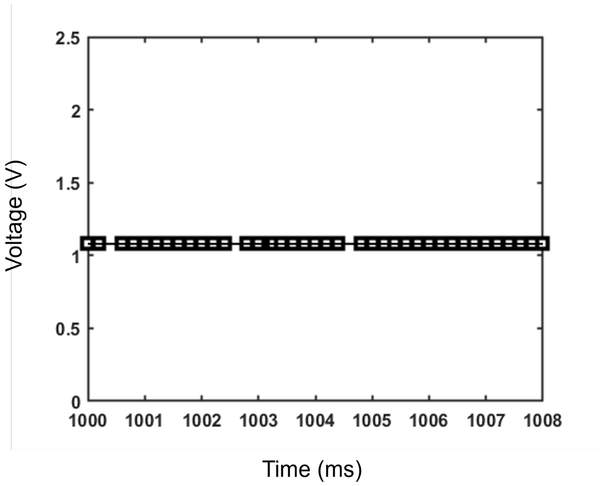

(a) V_OUT

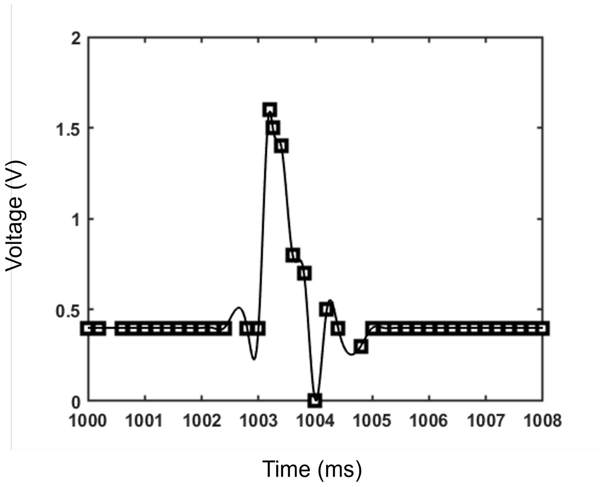

(b) V_LX

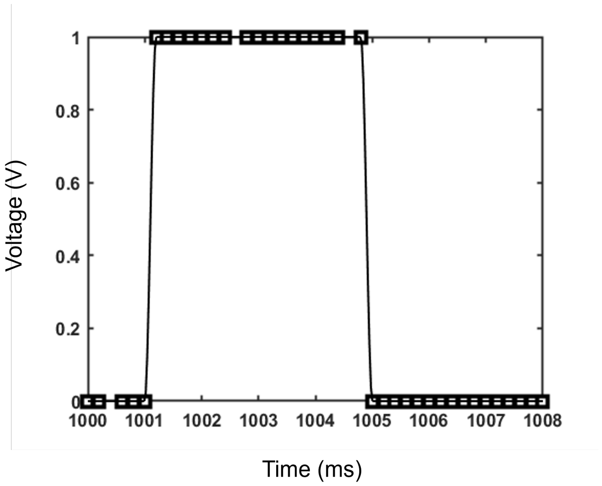

(c) EN_DEL

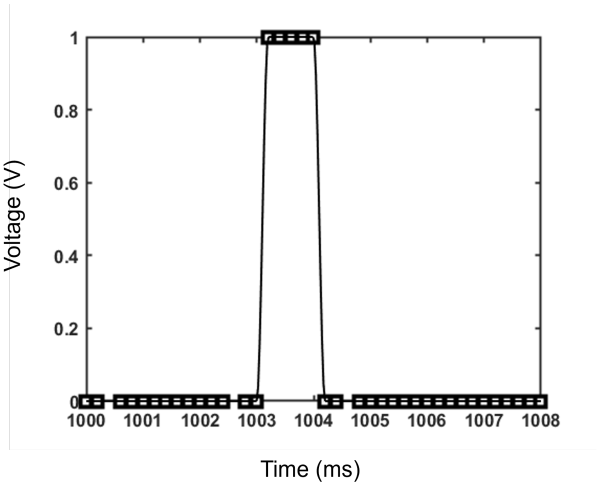

(d) ZCDB

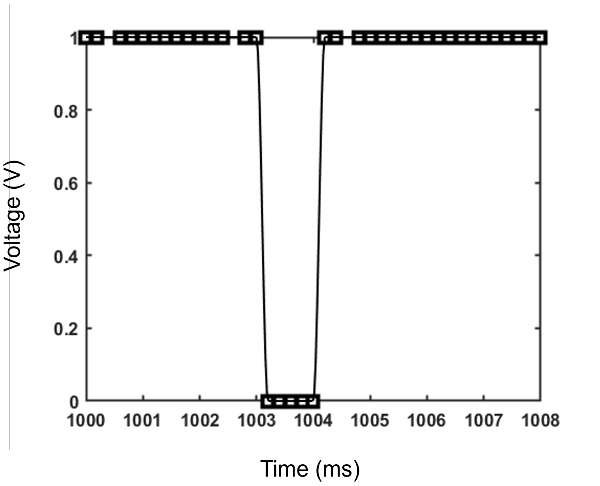

(e) SWPMOS

Figure 3.22: High-side switch control waveforms.

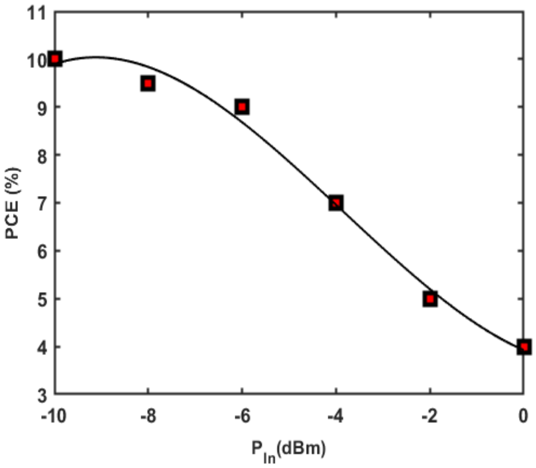

Figure 3.23: Simulated efficiency of overall RF energy harvesting system.

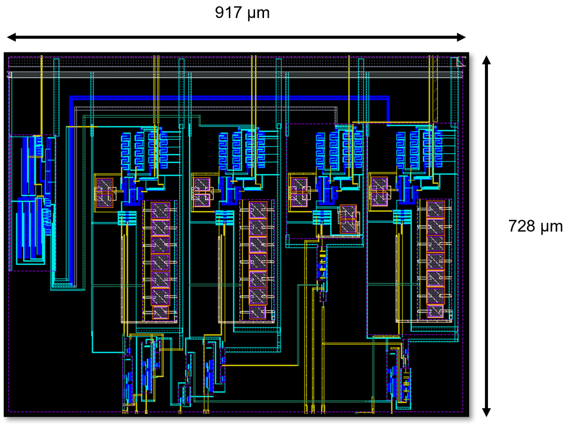

(a) Layout

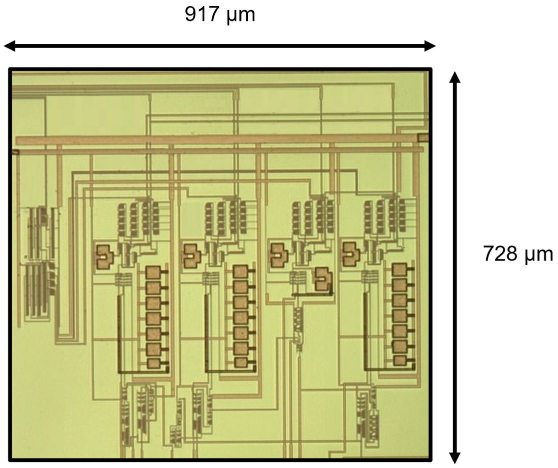

(b) Chip Micro-photograph

Figure 3.24: Layout and chip micro-photograph of boost converter.

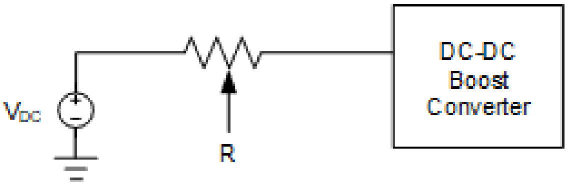

Figure 3.25: Equivalent circuit of RF rectifier.

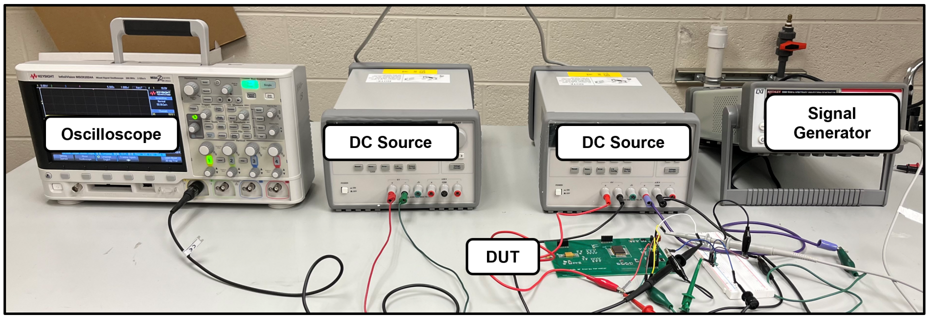

Figure 3.26: Test set-up of DC-DC converter.

RF rectifier model as demonstrated in Fig. 3.25. The equivalent circuit consists of a DC voltage, V_{DC} and a variable resistor, R. The DC voltage, V_{DC} varies from 0.62 V to 0.78 V and the variable resistor, R varies from 10 KΩ to 20 KΩ.

Fig. 3.26 demonstrates the test set-up of the DC-DC boost converter. From Fig. 3.27, it can be observed that the RF energy harvesting produces 1.01 V output voltage during testing at -10 dBm of input power which is close to the simulation results.

3.6 Maximum Power Point Tracking (MPPT) Controller

3.6.1 FOCV Based Maximum Power Point Tracking

According to the maximum power transfer theorem if the load impedance matches the output impedance of the source, maximum power will be transferred from the source to the load. Additionally, it has been demonstrated in Section 3.4 that the proposed active rectifier has the maximum efficiency for an optimal load impedance. As the optimal load impedance of the rectifier at specific available input power is known, the converter needs to be connected to the rectifier with optimum input impedance so that the impedances between them are matched. Therefore, the maximum available power will be transferred from the rectifier to the converter.

The DC-DC boost converter in the proposed system is being operated in discontinuous conduction mode (DCM). The simplified equation of the input impedance of the boost converter can be expressed

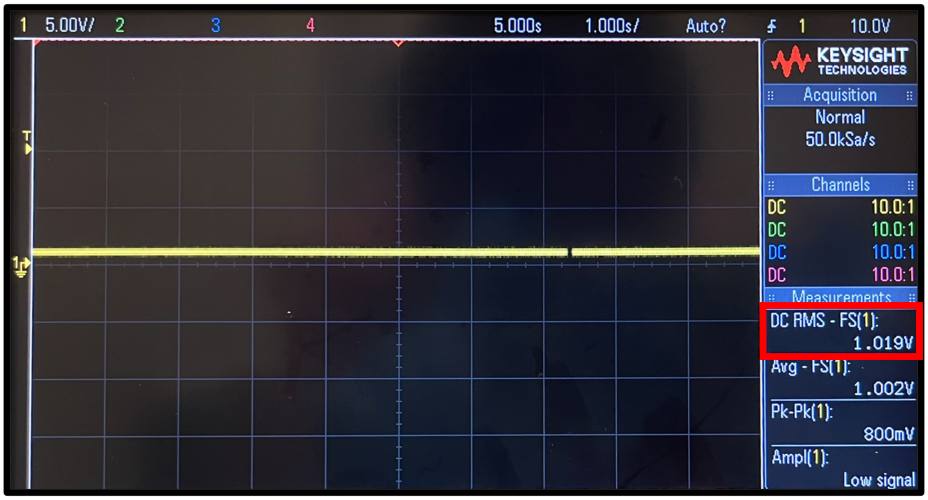

Figure 3.27: Output voltage of boost converter.

as:

$$Z_{IN} = \frac{V_{IN}}{I_{L-avg}} = \frac{2L}{t_1^2 f_s} \tag{3.15}$$

From equation (3.15), it can be observed that by controlling the NMOS switching signal (t_1) of the converter, its input impedance can be controlled.

Maximum power point tracking (MPPT) is an algorithm that is used to extract the maximum available power to the load under variable input power conditions. For the proposed rectifier, the maximum power point is the condition for optimum load impedance. It can also be observed from Section 3.4 that the optimal load impedance of the rectifier changes with variable input power conditions. Therefore, the maximum power point (MPP) of the rectifier needs to be tracked by using a suitable MPPT algorithm. Several MPPT algorithms are generally used to track MPP such as Perturb and Observe (P&O), Incremental Conductance (IC) and Fractional Open Circuit Voltage (FOCV) algorithm etc. Among these, FOCV algorithm estimates the values of the voltage MPP as a linear function of the open circuit output voltage of the rectifier and therefore is easier to implement. For the proposed system, the FOCV based MPPT algorithm have been applied to track the MPP of the system. Fig. 3.28 represents the FOCV based algorithm applied in the proposed system. At first, the open circuit output voltage of the rectifier is sampled. The maximum power point voltage (V_{MPP}) is estimated as a linear function of the open circuit output voltage. Then V_{MPP} voltage is compared with the input voltage of the converter (V_{IN}). If V_{MPP} is less than V_{IN}, then the NMOS switching signal (t_1) remains high and vice versa for V_{MPP} less than V_{IN}. Thus, the duty cycle is varied to set the input impedance of the DC-DC boost converter to an optimal value to extract the

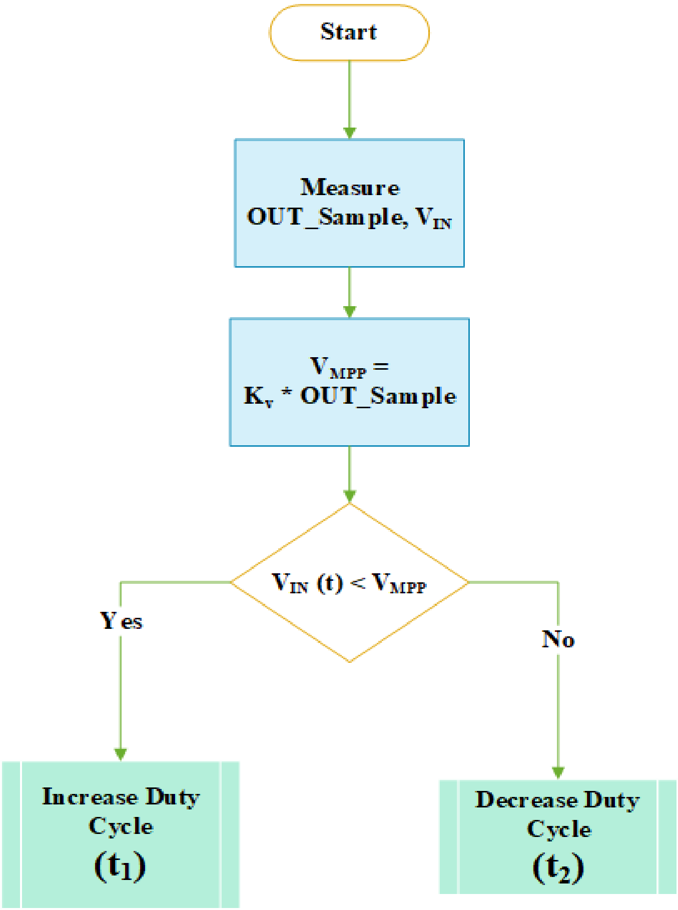

Figure 3.28: Applied FOCV based MPPT algorithm.

maximum available power from the converter.

Fig. 3.29 (a) and (b) represent the design and block diagram of the proposed MPPT scheme. The proposed MPPT controller consists of thee blocks:

- Sampling oscillator
- S&H circuit
- Comparator

Fig. 3.30 presents the schematic diagram of the proposed S&H circuit. The sampling frequency of the S&H circuit is 5 Hz which is provided by an oscillator (OSC). The sampling frequency of the S&H circuit is determined by the time required to store a proper open circuit output voltage of the rectifier into an external capacitor, C_1. The sampling frequency should be chosen carefully, so that the output voltage of the S&H circuit maintains the proper value in between the sampling periods. That means, during the boosting operation the leakage from C_1 should not affect the voltage sampled

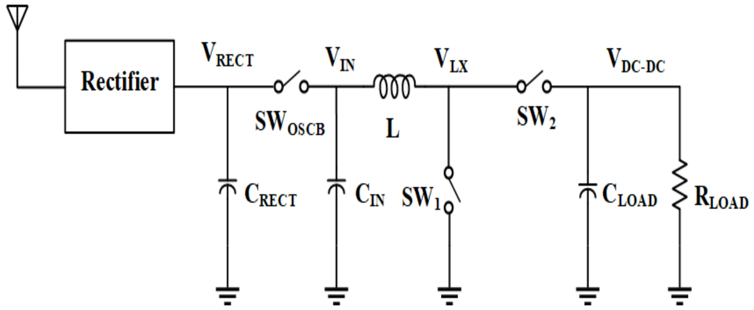

(a) Design

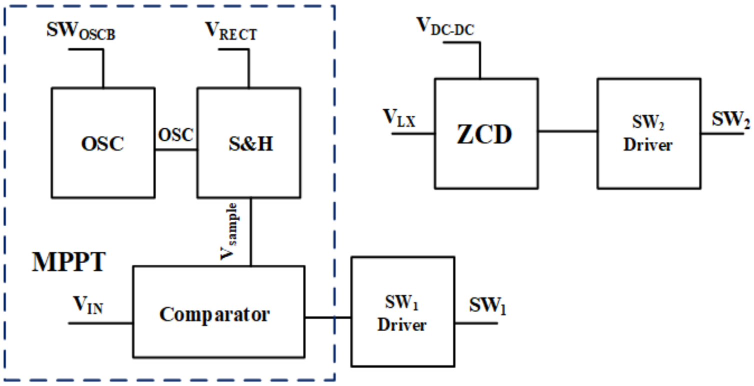

(b) Block diagram

Figure 3.29: Proposed MPPT scheme.

in C_1. If the sampled voltage if affected by the leakage from C_1, a proper value of reference voltage will not be obtained. Besides if the sampling operation is too frequent, the boosting operation will get interrupted and could cause improper operation of the converter. R_1 and R_2 are external resistors and their value needs to be set carefully to obtain proper reference voltage and to avoid drawing too much current from the rectifier voltage storage capacitor, C_{RECT}.

The current flowing through R_1 and R_2 is approximately 410 nA. As C_1 is external capacitor, R_3, R_4 and R_5 resistors are used to protect the input MOS transistor of the operational amplifier buffer as well as the source and the drain of the PMOS switch in the S&H circuit.

Since the S&H circuit is operating only during the sampling period, current consumption of the circuit needs to be minimized to optimize its static current consumption. In order to reduce the current consumption, an NMOS switch has been used in the S&H circuit which is controlled by the OSC signal. Therefore, the current consumption of the S&H circuit is approximately 100 nA.

Fig. 3.31 (a) shows the low-side switch control scheme of the converter. The reference voltage, OUT_sample is compared to the input voltage of the converter (V_{IN}). The converter provides high value if OUT_sample voltage is higher than V_{IN}, otherwise it produces a low output signal. The

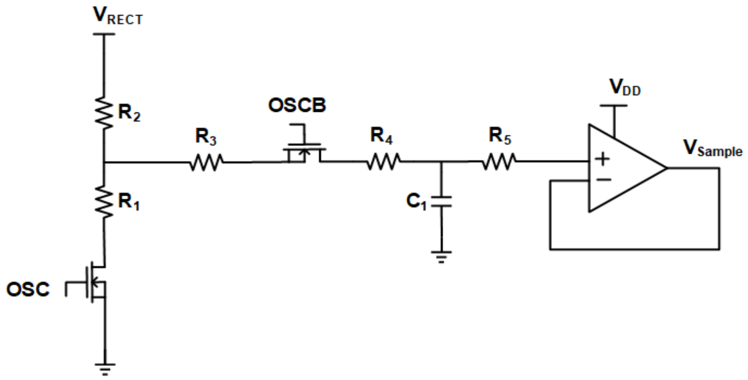

Figure 3.30: Schematic diagram of the proposed sample-and-hold circuit.

switching frequency of the DC-DC boost converter is determined by output signal of the comparator (SWN). Then the SWN signal is fed into an AND gate with OSCB signal to ensure that boosting operation is stopped during the sampling operation. The output signal of this AND gate needs to be fed into another AND gate with over voltage protection signal (OVP). The combined signal produces the control signal of low-side switch (SW_NMOS) of the converter.

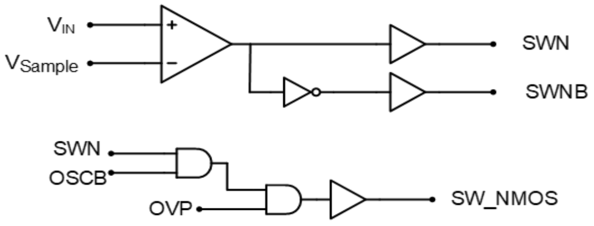

(a) Control circuit of low-side switch

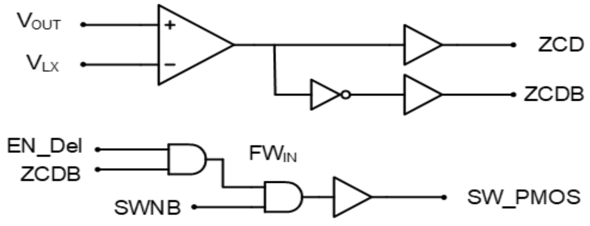

(b) Control circuit of high-side switch

Figure 3.31: DC-DC boost converter switch control scheme.

The high-side switch control scheme of the converter is shown in Fig. 3.31 (b). The high side-switch should be turned-off whenever the current through it crosses the zero point. If the high-side switch is not turned-off properly whenever the inductor completely discharges its stored energy, there will be a reverse current flow through the switch which can cause multiple problems. Generally, zero-current sensing circuits are required to detect whether the current through the inductor is

Table 3.3: Input impedance of the DC-DC boost converter (Simulated)

$P_{IN(dBm)}$	**L (μH)**	t_1 **(μs)**	f_s **(Hz)**	R_{RECT} **(kΩ)**	R_{IN} **(kΩ)**
-10	30	7.87	250	3.4 - 4.1	3.87
-7.5	30	7.86	316	2.4 - 3.1	3.07
-5	30	7.28	406	1.7 - 2.4	2.79
-2.5	30	6.95	478	1.4 - 1.9	2.60

crossing zero or not and these circuits are very complex. Therefore, a simplistic way of zero-current sensing is applied. Zero-current in an inductor means that the current stored in the inductor is fully discharged. Therefore, even though there exists some delay time between the zero inductor current and the zero voltage, the zero voltage of the inductor is detected because the switching frequency is low. A comparator has been applied which compares the output voltage of the DC-DC boost converter (V_{OUT}) to the inductor node voltage (V_{LX}). Whenever V_{LX} goes below V_{OUT}, the inductor is considered to be fully discharged and the high-side switch is turned-off immediately.

3.6.2 Machine Learning Based Maximum Power Point Tracking

The proposed fractional open circuit voltage (FOCV) based MPPT algorithm has a sampling frequency of 5 Hz. Therefore, under rapid input power varying condition, the FOCV based MPPT algorithm will suffer from poor tracking efficiency. To overcome this issue, a machine learning (ML) based MPPT algorithm has been implemented. The ML based MPPT controller tracks the maximum power point of the system by monitoring its input power (P_{in}), the input impedance (R_{IN}) and the input voltage (V_{IN}) of the converter. Setting the duty cycle corresponding to the maximum power point will allow the converter to be operated at the maximum power point. The proposed DC-DC boost converter has two main switches: SW_Low and SW_High. For the proposed case, the value of SW_High will be much lower compared to SW_Low. Thus modification of SW_Low will ensure the operation of the converter at the maximum power point. The output voltage of the converter V_{OUT} can be defined as Eq. 3.16 [31]:

$$\frac{V_{OUT}}{V_{IN}} = \frac{1}{1-D} \tag{3.16}$$

where, D is the duty cycle of the converter.

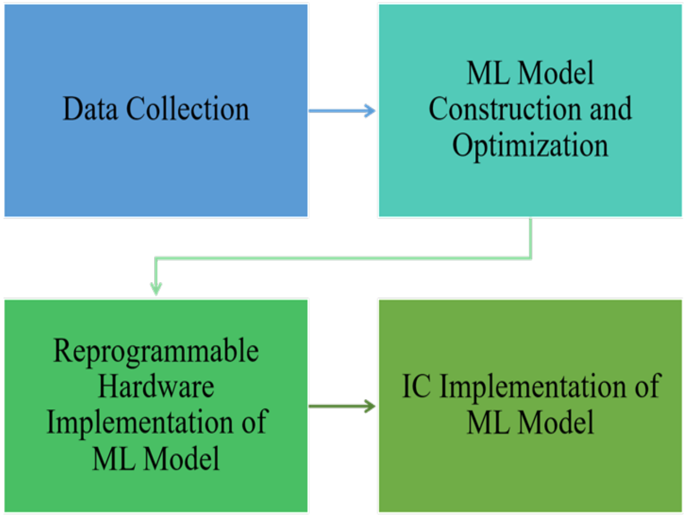

Figure 3.32: Design steps of the proposed ML based MPPT controller.

Fig. 3.32 demonstrates the design steps followed to develop the proposed ML based MPPT controller. At first, data is collected from the RF energy harvesting system [32]. An optimal ML model is developed and trained by using the collected data. After achieving optimal accuracy, the learned parameters such as weights and biases of the trained ML model are extracted. Then the optimal ML model is translated into hardware by using hardware descriptive language.

For training purpose, data was collected from FOCV integrated RF energy harvesting system. The input variables of the proposed ML model are the input power of the system, P_{in}, the input impedance of the converter, R_{IN} and the input voltage V_{IN}. The output of the ML model is the duty cycle (1/0) of te converter. 70% of collected data was used for training purpose while 30% data was used for testing.

Feed-forward neural networks (FNN) are well-known for their capability of non-linear mapping between the input and the output variables of the model. Besides, the algorithm used to map the non-linearity among variables is simplistic. The fundamental unit of FNN model is a neuron. By utilizing the mathematical function, the neuron approximates the relationship between the input and the output variable [33]. Thus, FNN model was selected for the proposed ML based MPPT controller. The one directional flow of information (from the input layer to the output layer) of FNN makes is suitable to be implemented into hardware.

For the proposed system, a three-layer FNN model as demonstrated in Fig. 3.33 was selected. Fig. 3.34 presents the proposed FNN algorithm. ML libraries such as scikit-learn and Keras were used to train the FNN model. For training, stochastic gradient descent (SGD) optimizer was applied

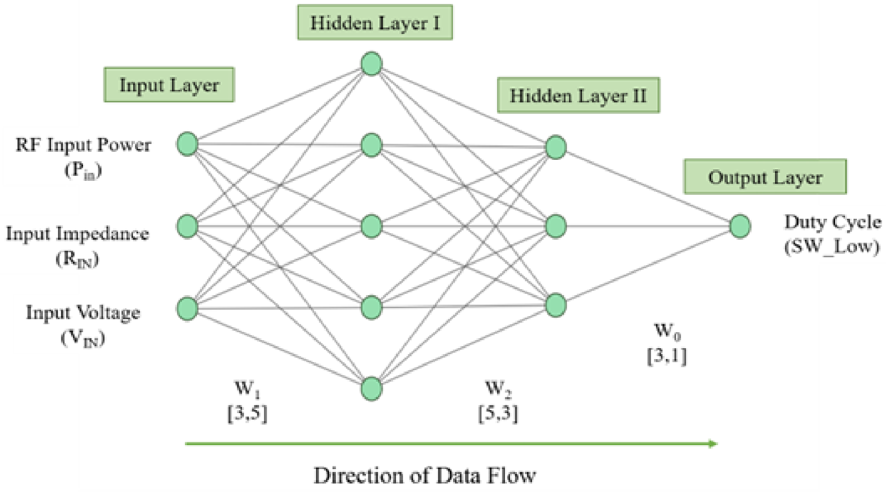

Figure 3.33: Proposed FNN model for tracking MPP.

Table 3.4: FNN model accuracy with various optimizers.

Optimizer	**Accuracy (%)**
Stochastic Gradient Descent	79.19
ADAM	73.93
RMSprop	74.61

to avoid overfitting. Learning of the developed FNN model was evaluated by mean square error (MSE) function.

Training and testing error plot of the FNN model is demonstrated in Fig. 3.35(a). With incrementing epochs, the learning of the FNN model is improved resulting in minimal error. From the figure it can be observed that the FNN model reaches to convergence at 500 epochs. In addition, Fig. 3.35(b) depicts learning of the FNN model with epochs. With incrementing epochs, the accuracy of the FNN model increases. The FNN model achieves 79.19% accuracy at 500 epochs.

To select the FNN model with optimal accuracy, it was trained by using different optimizers. The accuracy of the FNN model with various optimizers is presented in Table 3.4. The FNN model trained with stochastic gradient descent (SGD) optimizer achieved 79.19 % accuracy while the FNN trained with ADAM optimizer obtained 73.93 % accuracy and FNN trained with RMSprop optimizer obtained 74.61 % accuracy. As the FNN model trained with SGD demonstrated the highest accuracy, this model is considered to be optimal.

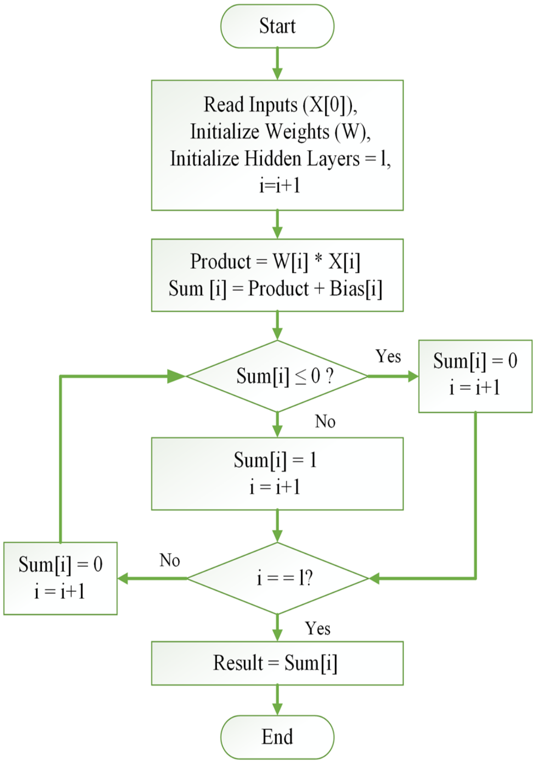

Figure 3.34: Proposed FNN algorithm for ML based MPPT controller.

The optimal FNN model was translated into hardware. The learned weights and biases of the optimal FNN model were extracted and utilized to develop the hardware FNN model. The fundamental operation of an FNN model includes addition and multiplication. In general, 32-bit floating-point library is used to perform such operations. Conversion of the learned parameters from 32-bit floating points to 8-bit integers helped reduce the power consumption. Among these 8-bits, the most significant bit (MSB) represents the sign-bit and rest of the bits represent data. Replacement of multipliers by shifters also resulted in significant reduction in power consumption.

To translate weights and biases of the optimized FNN model into logic blocks, hardware descriptive language, VHDL was used. For implementing the logic blocks into hardware Vivado HLx software was used. Fig. 3.36 shows the RTL level schematic of the FNN model. Fig. 3.37 demonstrates the components of a neuron. Table 3.5 demonstrates the device utilization comparison of several MPPT blocks implemented into hardware. From the table it can be concluded that the proposed hardware implemented FNN model utilizes approximately 17 times less LUT compared to [34] and [35] resulting is less power consumption.

Fig. 3.38 presents the simulation results of the hardware implemented FNN model. In this figure, 8-bit binary signals in red represent the input signals and 1-bit binary signal in pink represents the

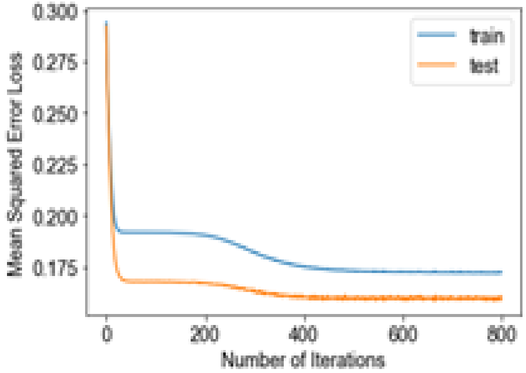

(a) Loss

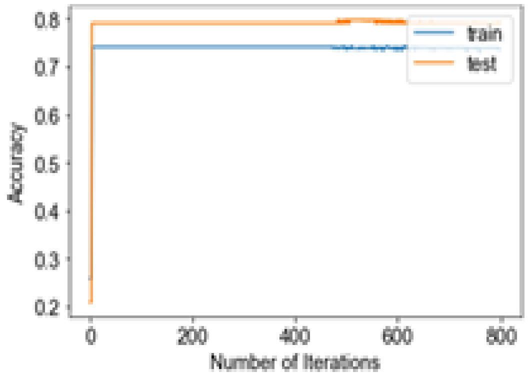

(b) Accuracy

Figure 3.35: Training and testing loss and accuracy of the FNN model.

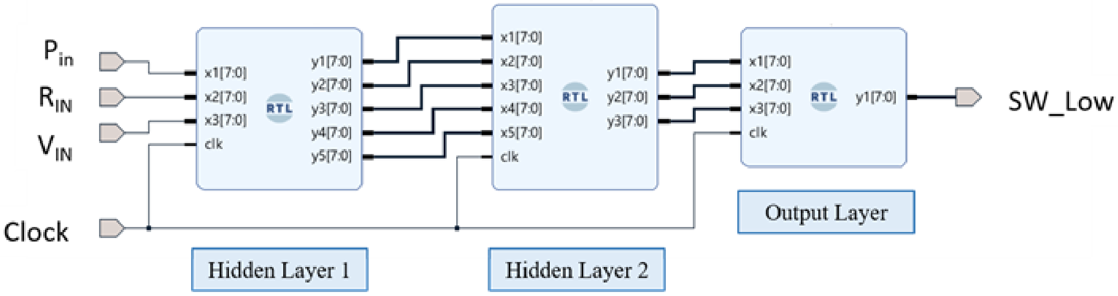

Figure 3.36: RTL view of the hardware implemented FNN based MPPT controller.

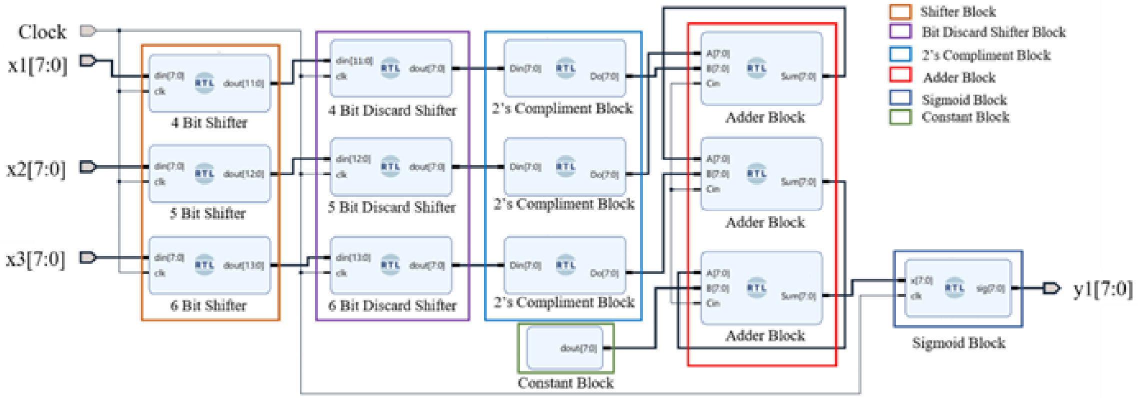

Figure 3.37: RTL view of the hardware implemented neuron components.

Table 3.5: A comparative study on hardware utilization of MPPT algorithms

Publications	**MPPT Algorithm**	**Resource**	**Utilization**	**Available**	**Utilization (%)**
This Work	Neural network	LUT	291	32600	0.89
This Work	Neural network	FF	204	65200	0.0.31
This Work	Neural network	IO	24	210	11.43
[34]	Fuzzy Logic	LUT	1928	10240	18
[34]	Fuzzy Logic	FF	2668	10240	26
[34]	Fuzzy Logic	IO	27	234	8
[35]	Neural Network	LUT	5029	28800	17
[35]	Neural Network	FF	-	-	-
[35]	Neural Network	IO	-	-	-
[36]	Fuzzy Logic	LUT	1336	63400	2
[36]	Fuzzy Logic	FF	11	1337	0.8
[36]	Fuzzy Logic	IO	15	210	7

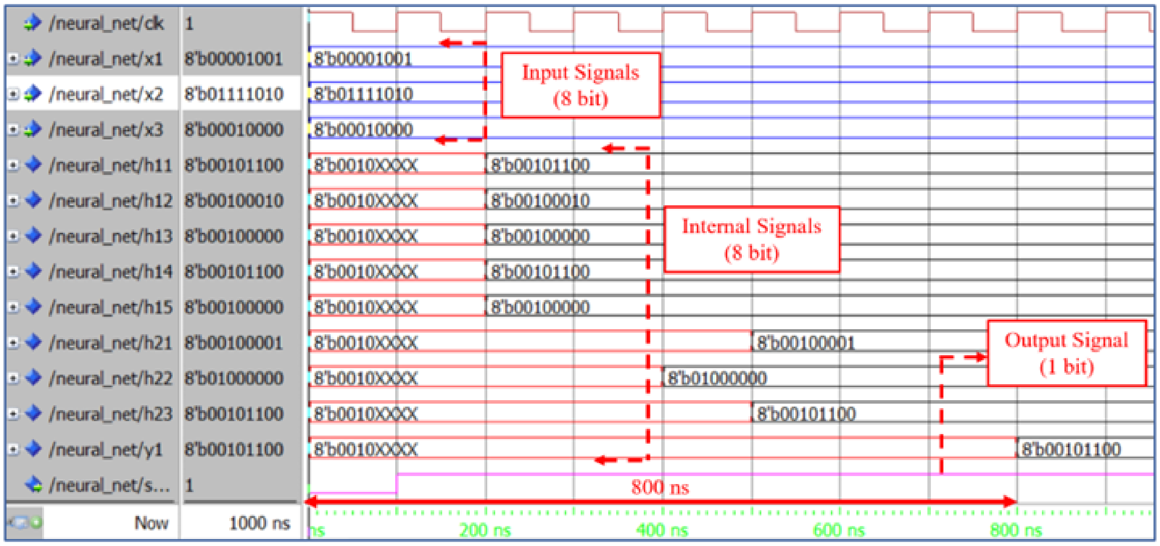

/neural_net/clk	1
/neural_net/x1	8'b00001001
/neural_net/x2	8'b01111010
/neural_net/x3	8'b00010000
/neural_net/h11	8'b00101100
/neural_net/h12	8'b00100010
/neural_net/h13	8'b00100000
/neural_net/h14	8'b00101100
/neural_net/h15	8'b00100000
/neural_net/h21	8'b00100001
/neural_net/h22	8'b01000000
/neural_net/h23	8'b00101100
/neural_net/y1	8'b00101100
/neural_net/s...	1
Now	1000 ns

Input Signals (8 bit)

Internal Signals (8 bit)

Output Signal (1 bit)

800 ns

Figure 3.38: Simulation results of the hardware implemented FNN model.

output signal of the FNN model. The dark red signal represents the clock signal which has a period of 10 ns with 50 % duty cycle. From the figure it can be observed that the response time of the FNN integrated MPPT controller is 800 ns reducing MPP tracking time by approximately 10^6 times. Therefore, it can be concluded that the proposed FNN integrated MPPT controller is able to track the maximum power point in real time.

Chapter 4

SELF-COMPENSATING RECTIFIER INTEGRATED RF ENERGY HARVESTING SYSTEM

4.1 Design of Self-Compensating Rectifier Integrated RF Energy Harvesting System

Fig. 4.1 shows the proposed two-stage self-compensated rectifier. A cross-coupled topology based rectifier is implemented in order to dynamically bias the gates of the transistors. In this toplogy, the bias voltage is in the opposite phase of the input signal. In the case of a PMOS transistor, when a positive input signal is rectified, the bias voltage becomes negative thereby compensating the threshold voltage and reducing the forward voltage drop. In the case of a negative input signal being rectified, the bias voltage at the gate of the PMOS transistor becomes positive. This in-turn increases the effective threshold voltage resulting in reduced reverse leakage current.

Applied dynamic bias compensation technique increases the efficiency of the rectifier. However, in this case the bias voltage is limited by the amplitude of the input signal. For very low input power, the bias voltage becomes lower than the threshold voltage. Therefore, only dynamic biasing technique

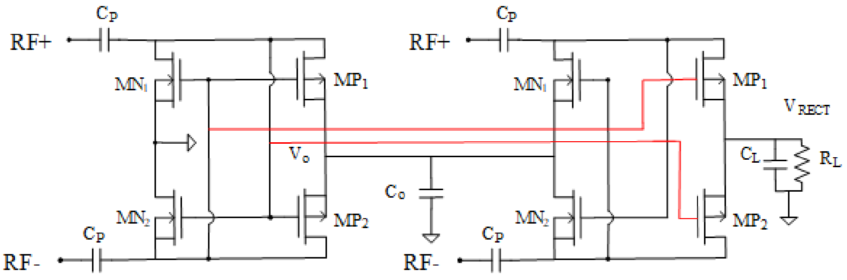

Figure 4.1: Schematic diagram of the proposed self-compensating RF rectifier.

based rectifier will not be sufficient to perform well with ultra low input RF signals. Therefore, a static bias compensation has been added to the dynamic bias compensation.

In Fig. 4.1 the transistors MN_1 and MN_2 zero V_T NMOS transistors. This implies that the NMOS transistors have threshold voltage near 0 V and therefore do not need threshold voltage compensation. Transistors MP_1 and MP_2 are low voltage PMOS transistors and there bias compensation is required in order to reduce the forward voltage drop for PMOS transistors. In this static bias technique, the gate of PMOS transistors is connected to the same point as in the dynamic biasing technique. However, the signal from the previous stage will be connected for this purpose. After applying this technique, the AC component of the obtained bias voltage is the same as the dynamic biasing, but the DC level is lowered by V_{OUT}/N.

4.2 Simulation Results of Self-Compensating Rectifier Integrated RF Energy Harvesting System

Fig. 4.2 depicts the efficiency of the rectifier with respect to various load impedances for different input powers. From the figure, it can be observed that the efficiency of the rectifier changes with the variation of the input power. Additionally it can be found that that the efficiency of the rectifier changes with the change in the load impedance. For -10 dBm input power demonstrated in Fig. 4.2 (a) it can be observed that with the increment of the load resistance the efficiency of the rectifier increases. For -10 dBm input power, the rectifier provides the highest efficiency of 72.5% at 11 kΩ load impedance. Besides it can be observed that the rectifier operates above 60% efficiency for the load impedance range of 6.2 kΩ - 20 kΩ. On the other hand, at 0 dBm input power the rectifier operates with 50.75% efficiency with 5 kΩ load impedance. The rectifier operates with the lowest efficiency of 27.33% with 11 kΩ load impedance. Therefore, it is crucial to find the optimal load impedance so that the rectifier operates with proper efficiency for the input power range -10 dBm to 0 dBm. After carefully observing the performance of the rectifier for various load impedances for the input power range of -10 dBm to 0 dBm, 11 kΩ load impedance has been chosen to be the optimal.

Fig. 4.3 shows the output voltage, V_{RECT} for various input powers, P_{IN} and for various load conditions, R_L of the proposed rectifier. With the increment of the input power, the output voltage of the rectifier increases. Also, with the increment of load resistance, the output voltage of the rectifier increases. The proposed rectifier provides the maximum output voltage of 1.734 V for 11 kΩ resistive load at 0 dBm input power. The rectifier produces the minimum output voltage of 0.525 V

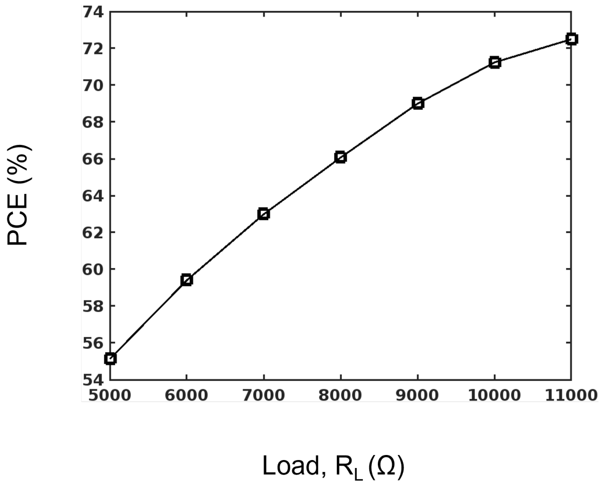

(a) Efficiency at -10 dBm

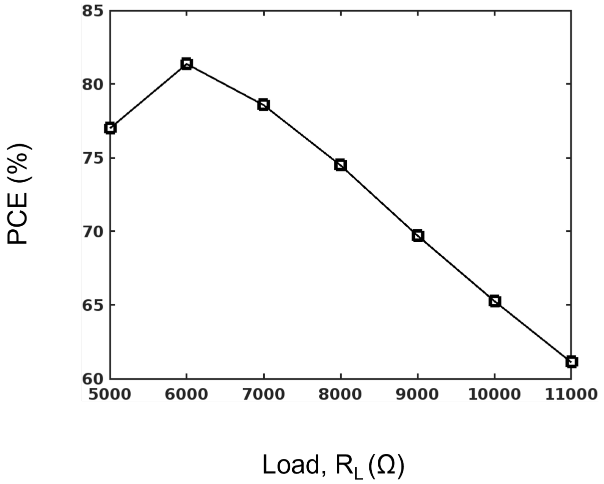

(b) Efficiency at -8 dBm

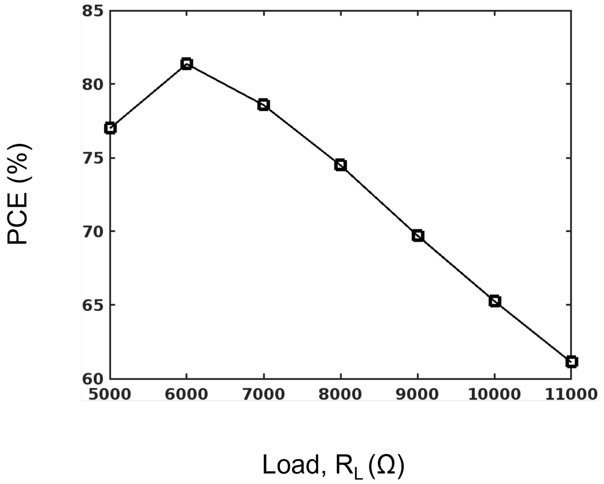

(c) Efficiency at -6 dBm

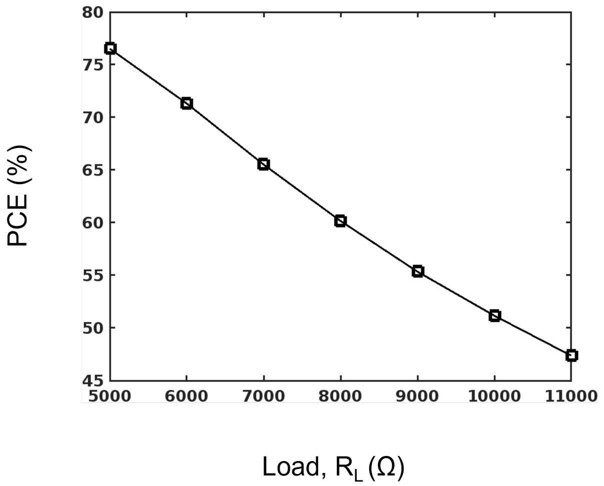

(d) Efficiency at -4 dBm

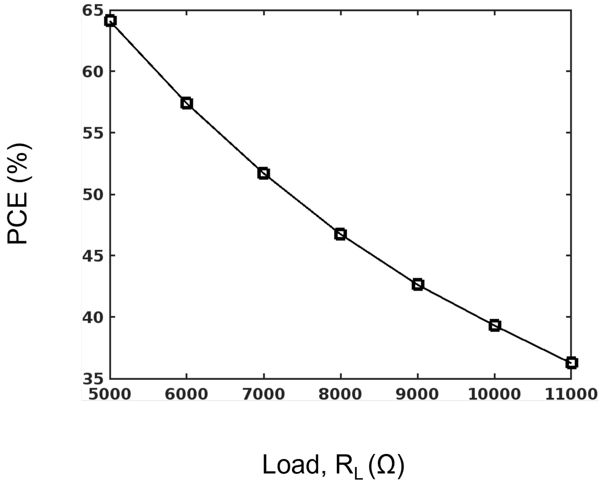

(e) Efficiency at -2 dBm

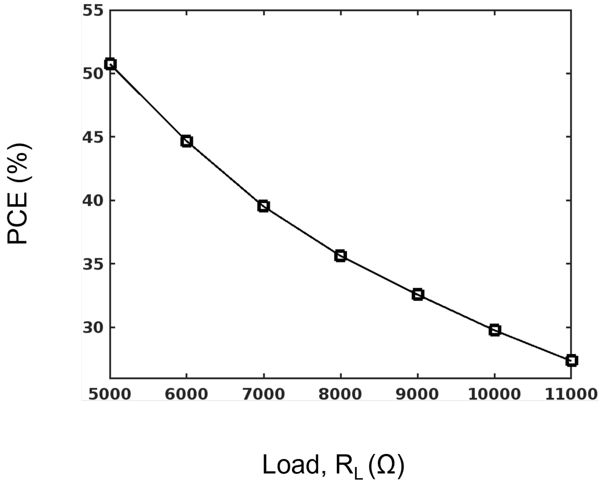

(f) Efficiency at 0 dBm

Figure 4.2: Efficiency of the proposed rectifier with various input power, P_{IN} and load conditions, R_L.

Table 4.1: Performance summary and comparison

Parameters	[37]	[38]	[39]	**This Work**
Technology	130 nm	130 nm	180 nm	180 nm
Frequency	915 MHz	902-928 MHz	830 MHz	900 MHz
Architecture	Self-comp.	Ada. V_{th} comp.	Diff. rect.	Self-comp.
Output Voltage	2.32 V	3.2 V	2 V	1 V
Max PCE	42.8% @-16 dBm	32% @-15 dBm	44.1% @-17 dBm	74.8% @-8 dBm

for 5 kΩ resistive load at -10 dBm input power.

Fig. 4.4 showcases the PCE of the proposed rectifier for various RF input power levels with 11 kΩ load. At -10 dBm input power, the rectifier operates with 72.5% efficiency. The rectifier performs with the maximum efficiency of 74.8% at -8 dBm input power. From the figure it can be observed that with the increment of the input power, the efficiency of the rectifier is decreased. The rectifier operates with the lowest efficiency of 27.3% at 0 dBm input power. As the proposed rectifier was designed using cross-connected topology, the shoot-through current will be increased with the increment of the input power resulting in lower efficiency.

Table 4.1 shows a performance summary of the proposed work and comparison with state-of-the-art works in RF energy harvesting. Among the existing designs, the proposed architecture achieves a peak efficiency of 74.8% at-8 dBm, and the efficiency is above 50 % between-10 dBm to-6 dBm. The proposed rectifier is able to produce output voltage more than 1 V for the input power range -10 dBm to 0 dBm. Therefore, this RF energy harvesting system can be connected directly to the loads and additional DC-DC conversion circuit is not required. Therefore, the overall peak efficiency remains to be 74.8% at -8 dBm which is very high compared to the other reported energy harvesting systems.

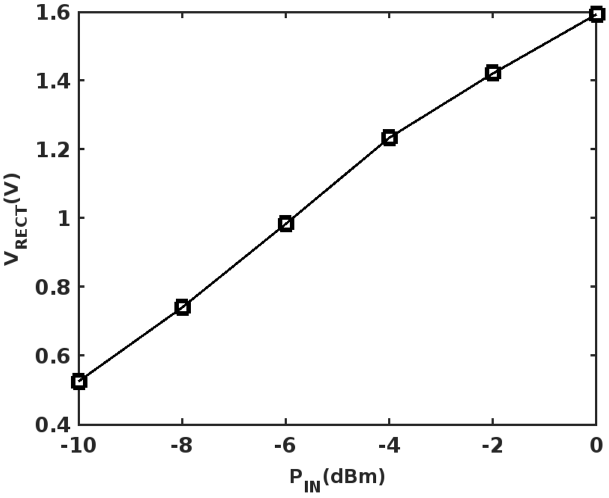

(a) V_{RECT} at with 5 kΩ load impedance

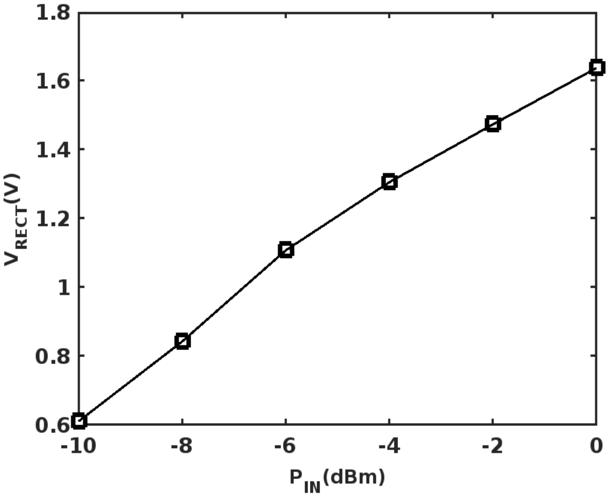

(b) V_{RECT} at with 6 kΩ load impedance

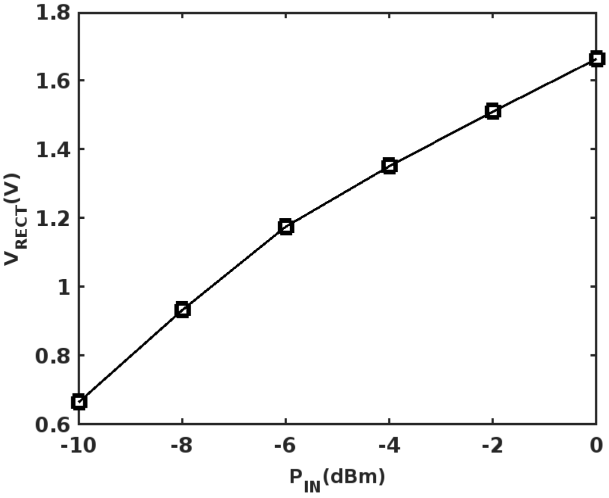

(c) V_{RECT} at with 7 kΩ load impedance

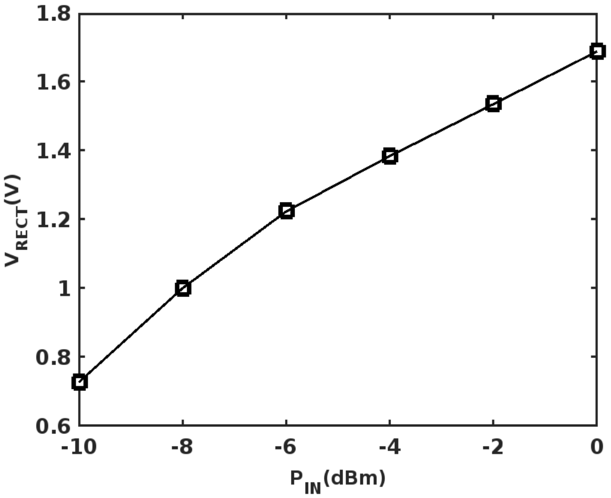

(d) V_{RECT} at with 8 kΩ load impedance

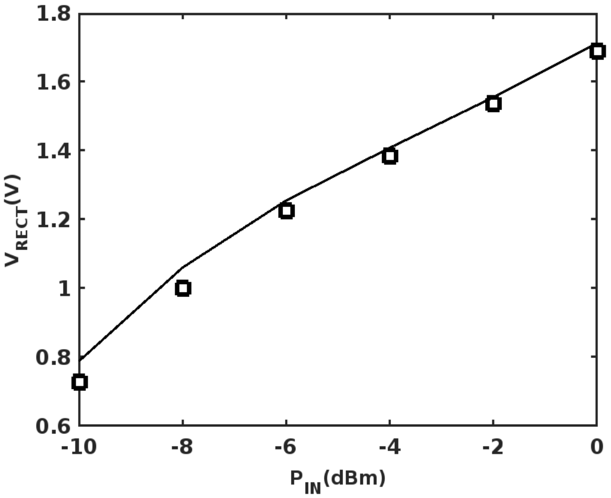

(e) V_{RECT} at with 9 kΩ load impedance

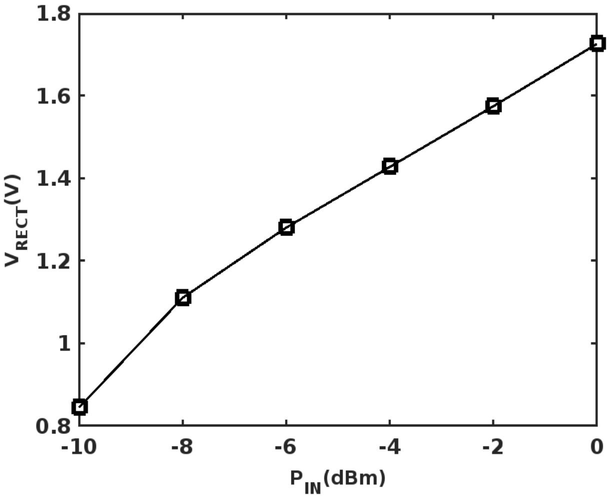

(f) V_{RECT} at with 10 kΩ load impedance

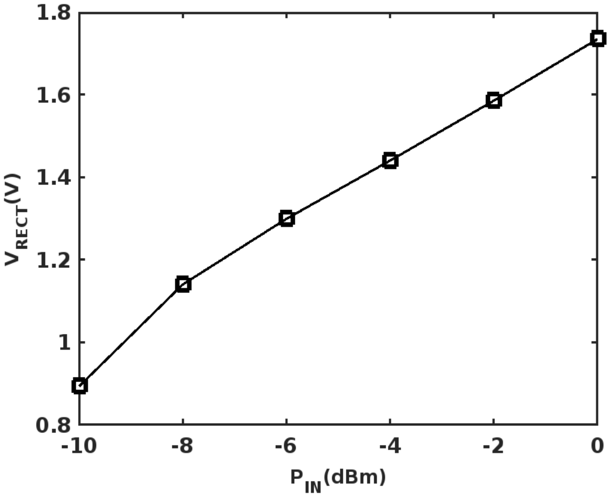

(g) V_{RECT} at with 11 kΩ load impedance

Figure 4.3: Output voltage of the rectifier, V_{RECT} with respect to input power, P_{IN} for various load impedances, R_L

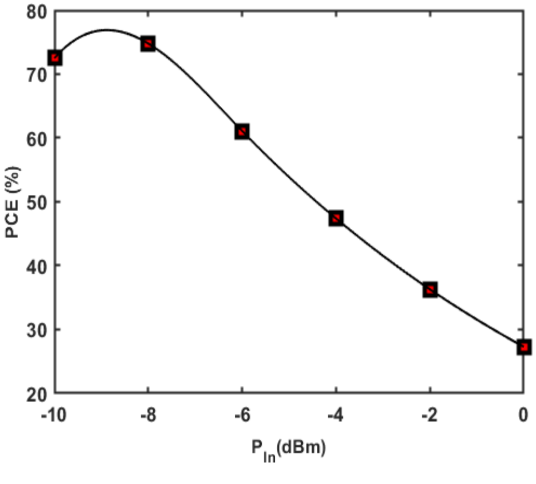

Figure 4.4: PCE of the proposed RF rectifier with respect to various input power, P_{IN}.

Chapter 5

CONCLUSION & FUTURE WORK

5.1 Conclusion

In this dissertation, a radio-frequency based energy harvesting systems have been presented. The proposed system showed the new approach of maximum power point tracking (MPPT). Unlike previously reported RF energy harvesting systems with A/D converter (ADC) as the main controlling source of MPPT, the proposed MPPT system is composed with simple resistive network with storage capacitor and buffer. With this simple design, the proposed MPPT system does not require any calibration whenever the system is powered off. The conventional MPPT system with ADC actually requires calibration if there is no stored calibration data such as MCU or memory. In addition, the proposed system consumes only less than 1 µA of current which is substantially less than the typical ADC controlled MPPT systems.

One of the major concerns while designing the RF energy harvesting system is the rapid input power variation due to the unpredictable RF sources. Traditional MPPT algorithm shows degraded performance with rapid input power variation. In order to further enhance the performance of the MPPT controller during rapid input power variation, a machine learning based MPPT controller is presented. The machine learning algorithm has been translated into VHDL and has been implemented into FPGA. The device utilization percentage of the proposed machine learning model is approximately 17 times lower than that of the other reported works in literature. Besides the hardware implemented ML model has very fast response time of 800 ns making the MPPT controller a real-time MPPT tracker.

Finally, a two-stage self-compensated rectifier integrated RF energy harvesting system is presented. In the proposed scheme, dynamic biasing along with static-compensation technique resulted in high peak PCE of 74.8% at -8 dBm input power. Besides, the proposed circuit produces sufficient output voltage (greater than 1V) eliminating the need to add another DC-DC converter. The proposed energy harvesting system can be directly integrated with loads such as IoT sensor nodes as well as to increase the battery lifetime of low-power biomedical devices.

5.2 Future Work

Antenna design of the RF energy harvesting system was out of scope for this research. In future, the proposed RF energy harvesting systems should be integrated with various efficient antenna models to further measure and analyze the performance.

For future research purpose, the proposed architecture should be designed and implemented for multi-band RF energy harvesting system using adjustable matching circuits. This will validate the use of proposed RF energy harvester for various frequencies. Besides the proposed matching network consists of inductors and thus off-chip components needs to be added to the energy harvesting system. Replacement of inductors with capacitors will eliminate the necessity of off-chip components making the system more compact.

Additionally, the machine learning based MPPT controller should be implemented into circuit in order to study the test performance of the proposed design. In addition to that, other machine learning based algorithms and hybrid algorithms should be designed for RF energy harvesting system to explore optimal MPPT algorithm for such system. Additionally these algorithms should be implemented into hardware to ensure minimal power consumption.

LIST OF ILLUSTRATIONS

LIST OF TABLES

BIBLIOGRAPHY

[1] I. E. Agency, *Key World Energy Statistics 2010*, 2010. [Online]. Available: https://www.oecd-ilibrary.org/content/publication/9789264095243-en

[2] "Key world energy statistics 2021," https://iea.blob.core.windows.net/assets/52f66a88-0b63-4ad2-94a5-29d36e864b82/KeyWorldEnergyStatistics2021.pdf, accessed: 2021-12-05.

[3] "U.s. energy facts explained," https://www.eia.gov/energyexplained/us-energy-facts/, accessed: 2022-05-10.

[4] "Energy_2021_united-states_0.png," https://flowcharts.llnl.gov/sites/flowcharts/files/2022-04/Energy_2021_United-States_0.png, accessed: 2022-05-08.

[5] H. Ritchie, M. Roser, and P. Rosado, "Energy," *Our World in Data*, 2022, https://ourworldindata.org/energy.

[6] J. Singh, R. Kaur, and D. Singh, "Energy harvesting in wireless sensor networks: A taxonomic survey," *International Journal of Energy Research*, vol. 45, no. 1, pp. 118–140, 2021. [Online]. Available: https://onlinelibrary.wiley.com/doi/abs/10.1002/er.5816

[7] "Candle (tealight) powered teg with optional led light," https://www.tegmart.com/thermoelectric-generators/candle-powered-tealight-teg, accessed: 2020-02-22.

[8] "Cbmw provides an update on waste heat recovery projects; turbosteamer and the thermoelectric generator," https://www.greencarcongress.com/2011/08/bmwthermal-20110830.Html, accessed: 2019-03-20.

[9] F. Ali, W. Raza, X. Li, H. Gul, and K.-H. Kim, "Piezoelectric energy harvesters for biomedical applications," *Nano Energy*, vol. 57, pp. 879–902, 2019. [Online]. Available: https://www.sciencedirect.com/science/article/pii/S2211285519300126

[10] "Piezoelectricity," https://www.americanpiezo.com/knowledge-center/piezo-theory/piezoelectricity.html, accessed: 2020-01-28.

[11] X. Xu, D. Cao, H. Yang, and M. He, "Application of piezoelectric transducer in energy harvesting in pavement," *International Journal of Pavement Research and Technology*, vol. 11, no. 4, pp. 388–395, 2018, innovations in Pavement and Material Characterization and Modeling. [Online]. Available: https://www.sciencedirect.com/science/article/pii/S1996681417300408

[12] C. Covaci and A. Gontean, "Piezoelectric energy harvesting solutions: A review," *Sensors*, vol. 20, no. 12, 2020. [Online]. Available: https://www.mdpi.com/1424-8220/20/12/3512

[13] M. Prauzek, J. Konecny, M. Borova, K. Janosova, J. Hlavica, and P. Musilek, "Energy harvesting sources, storage devices and system topologies for environmental wireless sensor networks: A review," *Sensors*, vol. 18, no. 8, 2018. [Online]. Available: https://www.mdpi.com/1424-8220/18/8/2446

[14] S. Cao and J. Li, "A survey on ambient energy sources and harvesting methods for structural health monitoring applications," *Advances in Mechanical Engineering*, vol. 9, no. 4, p. 1687814017696210, 2017. [Online]. Available: https://doi.org/10.1177/1687814017696210

[15] S. Muhammad, J. J. Tiang, S. K. Wong, A. H. Rambe, I. Adam, A. Smida, M. I. Waly, A. Iqbal, A. S. Abubakar, and M. N. Mohd Yasin, "Harvesting systems for rf energy: Trends, challenges, techniques, and tradeoffs," *Electronics*, vol. 11, no. 6, 2022. [Online]. Available: https://www.mdpi.com/2079-9292/11/6/959

[16] "Integrated Radio Frequency Energy harvesting System," https://era.library.ualberta.ca/items/d50bda6a-648f-4991-a855-c9da9d01ff9d/view/c25677dd-bb76-4cb0-b9e4-5a5ae9c7a7c7/Zohaib-Hameed_Thesis.pdf, accessed: 2019-11-25.

[17] T. Le, K. Mayaram, and T. Fiez, "Efficient far-field radio frequency energy harvesting for passively powered sensor networks," *IEEE Journal of solid-state circuits*, vol. 43, no. 5, pp. 1287–1302, 2008.

[18] T.-W. Yoo and K. Chang, "Theoretical and experimental development of 10 and 35 ghz rectennas," *IEEE Transactions on Microwave Theory and Techniques*, vol. 40, no. 6, pp. 1259–1266, 1992.

[19] M. Basim, D. Khan, Q. U. Ain, K. Shehzad, S. A. A. Shah, B.-G. Jang, Y.-G. Pu, J.-M. Yoo, J.-T. Kim, and K.-Y. Lee, "A highly efficient rf-dc converter for energy harvesting applications

using a threshold voltage cancellation scheme," *Sensors*, vol. 22, no. 7, 2022. [Online]. Available: https://www.mdpi.com/1424-8220/22/7/2659

[20] K. V. G. Raghavendra, K. Zeb, A. Muthusamy, T. N. V. Krishna, S. V. S. V. P. Kumar, D.-H. Kim, M.-S. Kim, H.-G. Cho, and H.-J. Kim, "A comprehensive review of dc–dc converter topologies and modulation strategies with recent advances in solar photovoltaic systems," *Electronics*, vol. 9, no. 1, 2020. [Online]. Available: https://www.mdpi.com/2079-9292/9/1/31

[21] S. Maity, S. Ghosh, R. Pal, S. Saha, S. Samanta, S. Guha, R. Mondal, R. Sau, S. Pan, A. Das, and J. Maity, "Performance analysis of fuzzy logic controlled dc-dc converters," in *2019 International Conference on Communication and Signal Processing (ICCSP)*, 2019, pp. 0165–0171.

[22] V. Vorperian, "Simplified analysis of pwm converters using model of pwm switch. ii. discontinuous conduction mode," *IEEE Transactions on Aerospace and Electronic Systems*, vol. 26, no. 3, pp. 497–505, 1990.

[23] M. Sharma, A. Achra, V. Gali, and M. Gupta, "Design and performance analysis of interleaved inverter topology for photovoltaic applications," in *2020 International Conference on Power Electronics & IoT Applications in Renewable Energy and its Control (PARC)*. IEEE, 2020, pp. 180–185.

[24] S. D. Al-Majidi, M. F. Abbod, and H. S. Al-Raweshidy, "A modified p&o-mppt based on pythagorean theorem and cv-mppt for pv systems," in *2018 53rd International Universities Power Engineering Conference (UPEC)*. IEEE, 2018, pp. 1–6.

[25] D. Baimel, S. Tapuchi, Y. Levron, and J. Belikov, "Improved fractional open circuit voltage mppt methods for pv systems," *Electronics*, vol. 8, no. 3, p. 321, 2019.

[26] L. Bouselham, M. Hajji, B. Hajji, A. El Mehdi, and H. Hajji, "Hardware implementation of fuzzy logic mppt controller on a fpga platform," in *2015 3rd International Renewable and Sustainable Energy Conference (IRSEC)*. IEEE, 2015, pp. 1–6.

[27] "MS Windows NT kernel description," http://wera.cen.uni-hamburg.de/DBM.shtml, accessed: 2010-09-30.

[28] I. A. Echearte, D. J. López, M. G. Forner, F. Giuppi, and A. T. Georgiadis, "A high-efficiency matching technique for low power levels in rf harvesting," 2013.

[29] A. Shameli, A. Safarian, A. Rofougaran, M. Rofougaran, and F. De Flaviis, “Power harvester design for passive uhf rfid tag using a voltage boosting technique,” *IEEE Transactions on Microwave Theory and Techniques*, vol. 55, no. 6, pp. 1089–1097, 2007.

[30] Y. Lu, H. Dai, M. Huang, M.-K. Law, S.-W. Sin, S.-P. U, and R. P. Martins, “A wide input range dual-path cmos rectifier for rf energy harvesting,” *IEEE Transactions on Circuits and Systems II: Express Briefs*, vol. 64, no. 2, pp. 166–170, 2017.

[31] L. Bouselham, M. Hajji, B. Hajji, A. El Mehdi, and H. Hajji, “Hardware implementation of fuzzy logic mppt controller on a fpga platform,” in *2015 3rd International Renewable and Sustainable Energy Conference (IRSEC)*, 2015, pp. 1–6.

[32] T. Oh, D. Parvin, O. Hassan, S. Shamsir, and S. K. Islam, “Mppt integrated dc–dc boost converter for rf energy harvester,” *IET Circuits, Devices & Systems*, vol. 14, no. 7, pp. 1086–1091, 2020. [Online]. Available: https://ietresearch.onlinelibrary.wiley.com/doi/abs/10.1049/iet-cds.2019.0509

[33] P. G. Asteris, P. C. Roussis, and M. G. Douvika, “Feed-forward neural network prediction of the mechanical properties of sandcrete materials,” *Sensors*, vol. 17, no. 6, 2017. [Online]. Available: https://www.mdpi.com/1424-8220/17/6/1344

[34] A. Messai, A. Mellit, A. M. Pavan, A. Guessoum, and H. Mekki, “Fpga-based implementation of a fuzzy controller (mppt) for photovoltaic module,” *Energy conversion and management*, vol. 52, no. 7, pp. 2695–2704, 2011.

[35] F. Chekired, A. Mellit, S. A. Kalogirou, and C. Larbes, “Intelligent maximum power point trackers for photovoltaic applications using fpga chip: A comparative study,” *Solar Energy*, vol. 101, pp. 83–99, 2014.

[36] M. Y. Allani, D. Mezghani, F. Tadeo, and A. Mami, “Fpga implementation of a robust mppt of a photovoltaic system using a fuzzy logic controller based on incremental and conductance algorithm,” *Engineering, Technology amp; Applied Science Research*, vol. 9, no. 4, p. 4322–4328, Aug. 2019. [Online]. Available: https://etasr.com/index.php/ETASR/article/view/2771

[37] S. M. Noghabaei, R. L. Radin, Y. Savaria, and M. Sawan, “A high-efficiency ultra-low-power cmos rectifier for rf energy harvesting applications,” in *2018 IEEE International Symposium on Circuits and Systems (ISCAS)*. IEEE, 2018, pp. 1–4.

[38] Z. Hameed and K. Moez, “A 3.2 v–15 dbm adaptive threshold-voltage compensated rf energy harvester in 130 nm cmos,” *IEEE Transactions on Circuits and Systems I: Regular Papers*, vol. 62, no. 4, pp. 948–956, 2015.

[39] P.-H. Hsieh, C.-H. Chou, and T. Chiang, “An rf energy harvester with 44.1% pce at input available power of-12 dbm,” *IEEE Transactions on Circuits and Systems I: Regular Papers*, vol. 62, no. 6, pp. 1528–1537, 2015.

VITA

Dilruba Parvin completed her bachelors' degree in Electrical, Electronics and Communication Engineering (EECE) from Military Institute of Science and Technology (MIST) in 2016. Currently she is pursuing her doctorate degree in Electrical and Computer Engineering at University of Missouri. She is working simultaneously in Analog/Mixed-Signal, VLSI and Devices Laboratory (AVDL) as a research assistant and in the department of Electrical Engineering and Computer Science (EECS) as a graduate instructor. She also served EECS department as a graduate teaching assistant for two years. Dilruba's research topic focuses on the development of low-power integrated circuits for RF energy harvesting applications. Additionally, she is working on the development of machine learning (ML) embedded energy efficient integrated circuits for energy harvesters. During her Ph.D. program, Dilruba has been awarded 2021 Outstanding Doctoral Student Award from the Department of EECS at the University of Missouri. She has been received Grace Hopper Celebration (GHC) Student Scholarship in 2020. In addition, she received the 1907 Women in Engineering award in 2019 from the Office of Diversity and Outreach Initiatives in the College of Engineering at the University of Missouri. She has been selected for Next Gen Circuit Designer 2022 Workshop and ISSCC 2022 Student Travel Grant.